JACS
JOURNAL OF THE AMERICAN CHEMICAL SOCIETY
pubs.acs.org/JACS
Article

Alkoxy-Substituted Quadrupolar Fluorescent Dyes

Yuanning Feng, Partha Jyoti Das, Ryan M. Young, Paige J. Brown, Jessica E. Hornick, Jacob A. Weber, James S. W. Seale, Charlotte L. Stern, Michael R. Wasielewski, and J. Fraser Stoddart*

Cite This: J. Am. Chem. Soc. 2022, 144, 16841−16854
Read Online
ACCESS | Metrics & More | Article Recommendations | Supporting Information

ABSTRACT: Polar and polarizable π-conjugated organic molecules containing push−pull chromophores have been investigated extensively in the past. Identifying unique backbones and building blocks for fluorescent dyes is a timely exercise. Here, we report the synthesis and characterization of a series of fluorescent dyes containing quadrupolar A−D−A constitutions (where A = acceptor and D = donor), which exhibit fluorescence emission at a variety of different wavelengths. We have investigated the effects of different electron-withdrawing groups, located at both termini of a *para*-terphenylene backbone, by steady-state UV/vis and fluorescence spectroscopy. Pyridine and substituted pyridinium units are also introduced during the construction of the quadrupolar backbones. Depending on the quadrupolarity, fluorescence emission wavelengths cover from 380 to 557 nm. Time-resolved absorption and emission spectroscopy reveal that the photophysical properties of those quadrupolar dyes result from intramolecular charge transfer. One of the dyes we have investigated is a symmetrical box-like tetracationic cyclophane. Its water-soluble tetrachloride, which is non-cytotoxic to cells up to a loading concentration of 1 μM, has been employed in live-cell imaging. When taken up by cells, the tetrachloride emits a green fluorescence emission without any hint of photobleaching or disruption of normal cell behavior. We envision that our design strategy of modifying molecules through the functionalization of the quadrupolar building blocks as chromophores will lead to future generations of fluorescent dyes in which these A−D−A constitutional fragments are incorporated into more complex molecules and polymers for broader photophysical and biological applications.

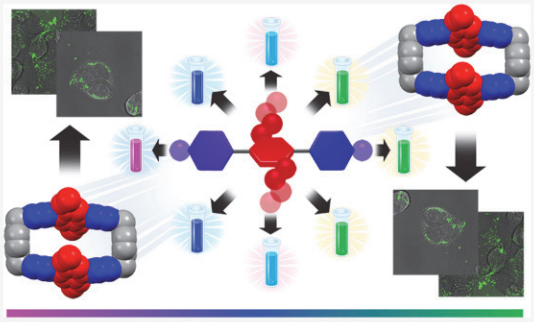

INTRODUCTION

Push−pull fluorescent dyes, which feature electron-donating (D) substituents connected to electron-accepting (A) substituents, have been investigated[1−9] as environmentally sensitive fluorophores. The design and synthesis of fluorescent organic compounds containing push−pull chromophores have emerged as an active area of research over the past two decades as a result of their potential applications in the fields of photovoltaics,[10−12] non-linear optics,[13,14] organic light emitting diodes,[15−18] fluorescent sensors,[19,20] and bioimaging.[21−24] Although quadrupolar chromophores,[25−42] which contain symmetrical structures, have no permanent dipole moment, experimental data[25−38,43−48] point to the existence of polar excited states. Time-resolved fluorescence (TRF) anisotropy measurements suggest that the initially delocalized excitation can be localized on the picosecond time-scale over one branch of the chromophore, leading to the formation of a polar state.

These push−pull fluorescent dyes show unique electronic and photonic features, which may be tuned and improved by straightforward synthetic modifications. Aromatic rings in those chromophores are π-conjugated, rendering their photophysical properties sensitive to the relative electron densities of each component. These electron densities can be modulated[49] by the introduction of a variety of substituents, that is, electron-donating groups (EDGs) and/or electron-withdrawing groups (EWGs). In addition, heterocyclic units have been introduced[25,45,50−57] into π-conjugated systems to modulate their photophysical and electrochemical properties. Extended bipyridinium-based cyclophanes[58−60] (Ex^nBox^{4+}) and their π-conjugated analogues[61−63] have been investigated extensively by us in the past. We consider box-like fluorescent tetracationic cyclophanes to be good candidates for biological imaging because of the excellent water solubility of their chloride salts and low cytotoxicity profiles based on our own previous investigations[63−70] carried out on tetra- and octacationic fluorescent cyclophanes,[63] cages,[65,66] and catenanes.[67−70]

Here, we report the rational design and synthesis of a series of fluorescent dyes which contain quadrupolar backbones as major building blocks. The acceptor−donor−acceptor (A−D−A) backbones all contain alkoxy-substituted electron-rich phenylene rings in their midriffs, with two electron-deficient rings, that is, (i) *para*-substituted phenylene, (ii) pyridine, or (iii) pyridinium units, connected symmetrically in a linear

Received: May 8, 2022
Published: September 9, 2022

Scheme 1. Synthesis of the Alkoxy-Substituted Quadrupolar Fluorescent Dyes, Namely, 1−6, 7·2PF$_6$, 8·2PF$_6$, and 9·4PF$_6$

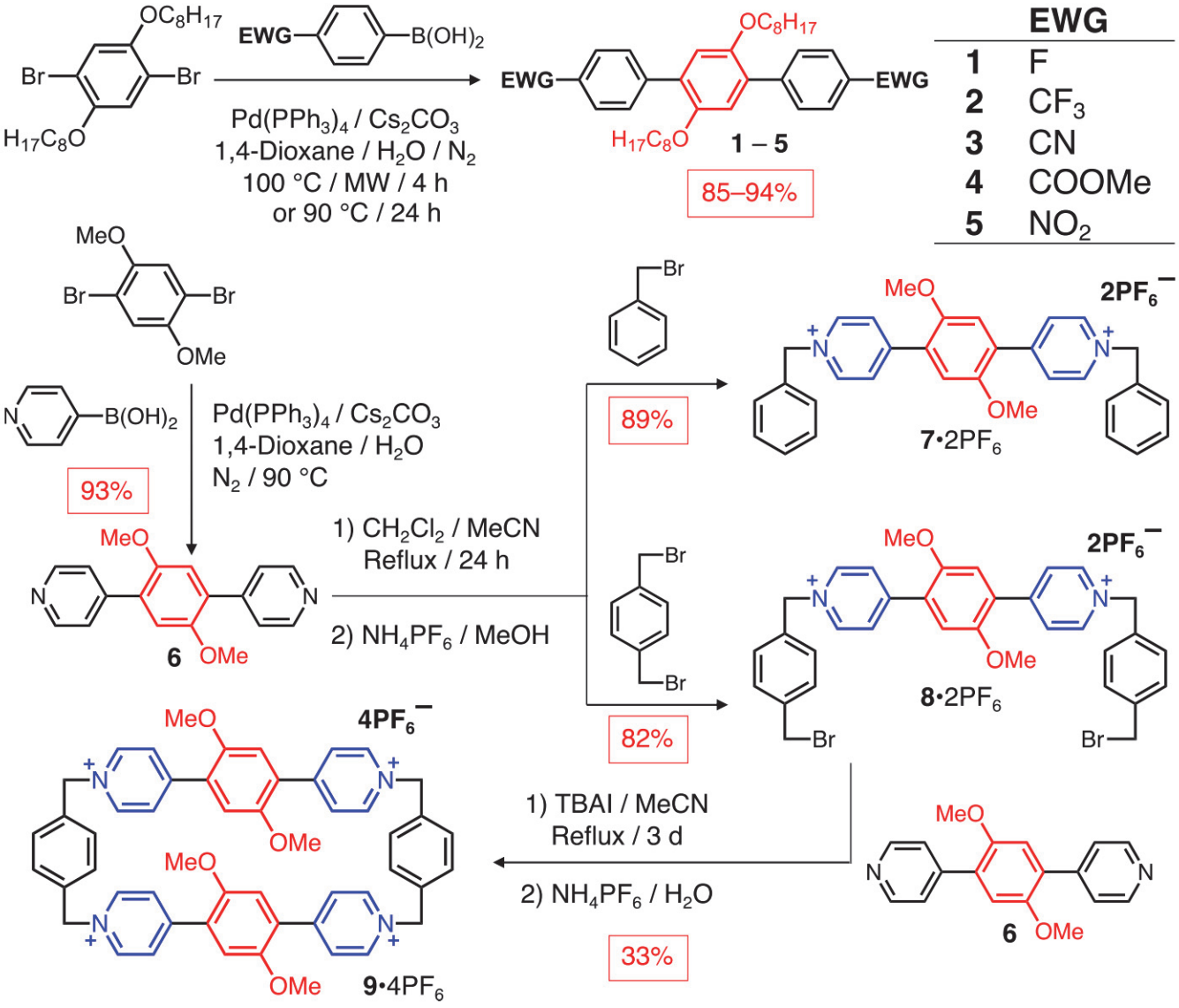

fashion by aryl−aryl single bonds. In dyes **1**−**5**, pairs of 2,5-substituted *n*-octyloxy chains, which are attached to the electron-rich donor rings (DRs), not only constitute a means of providing solubility and hydrophobicity but also act as EDGs. Five different *para*-substituted EWGs, from weaker to stronger, namely, F/CF_3/CN/COOMe/NO_2, were attached to the electron-deficient acceptor rings (ARs), affording fluorescent dyes **1**, **2**, **3**, **4**, and **5**, respectively. In dyes **6**, 7·2PF$_6$, **8**·2PF$_6$, **9**·4PF$_6$, and **9**·4Cl, 2,5-dimethyloxyphenylene units act as the DRs located in their midriffs, whereas pyridine rings and cationic pyridinium rings constitute the ARs located symmetrically at both ends. The dyes cover a wide range of both UV/vis absorption and fluorescence emission wavelengths, which are correlated to their quadrupolarity. Steady-state and time-resolved absorption and emission experiments were carried out to investigate the photophysical properties of both (i) neutral dyes **1**−**6** and (ii) cationic dye $\mathbf{9}^{4+}$ and its subunit $\mathbf{7}^{2+}$. In $\mathbf{9}^{4+}$, in particular, two quadrupolar building blocks are bridged by a pair of *para*-xylylene linkers, forming a rigid, box-like tetracationic cyclophane. This constitutionally symmetrical cyclophane is readily soluble both in polar organic solvents, for example, MeCN, Me_2CO, and DMF as its PF_6^- salt and in H_2O as its Cl^- salt. Investigations of their excited-state dynamics and mechanisms are indispensable for obtaining feedback and guidance about new optimal design and synthetic strategies. Cell experiments with the addition of the water-soluble tetrachloride **9**·4Cl were performed to probe its cytotoxicity profile: given its low toxicity, it was employed in confocal live-cell imaging experiments. Our investigations demonstrate that the cyclophane is readily taken up by cells at low treatment concentrations (as low as 1 μM) and can be easily imaged under conditions that sustain living cells.

EXPERIMENTAL SECTION

Synthesis. See Scheme 1. 1,4-Dioxane (5 mL) and H_2O (5 mL) were mixed and degassed using N_2. A mixture of 1,4-dibromo-2,5-dioctyloxybenzene (80 mg, 0.16 mmol), 4-fluorophenylboronic acid (61 mg, 0.44 mmol), $Pd(PPh_3)_4$ (27 mg, 0.023 mmol), and Cs_2CO_3 (259 mg, 0.795 mmol) was degassed under vacuum, followed by a N_2 flow cycle repeated three times. The degassed solvent was then injected into this mixture using a cannula. After reacting at 100 °C under a N_2 atmosphere in a microwave reactor for 4 h, the mixture was cooled to room temperature and the solvent was removed under

https://doi.org/10.1021/jacs.2c04906
J. Am. Chem. Soc. 2022, 144, 16841−16854

reduced pressure. The solid was re-dissolved in CH_2Cl_2 and washed with H_2O. After drying (Na_2SO_4), the solution was mixed with Celite545 and purified by column chromatography (SiO_2, hexane/EtOAc 49:1) to afford product **1** as a white solid (77 mg, 91%). ^{1}H NMR (500 MHz, $CDCl_3$): δ_H 7.63−7.50 (m, 4H), 7.16−7.06 (m, 4H), 6.94 (s, 2H), 3.90 (t, J = 6.4 Hz, 4H), 1.67 (p, J = 14.3, 6.5 Hz, 4H), 1.39−1.31 (m, 4H), 1.30−1.19 (m, 16H), 0.88 (t, J = 7.0 Hz, 6H). ^{13}C NMR (125 MHz, $CDCl_3$): δ_C 163.2, 161.2, 150.3, 134.4 (two overlapping peaks), 131.3, 131.2, 130.0, 116.3, 115.0, 114.9, 69.8, 31.9, 29.5, 29.4 (two overlapping peaks), 26.2, 22.8, 14.2. MS-APCI(+) (m/z): $[M]^+$ calcd for $C_{34}H_{44}F_2O_2$, 522.3304; found, 522.3311.

2. 1,4-Dioxane (5 mL) and H_2O (5 mL) were mixed and degassed using N_2. A mixture of 1,4-dibromo-2,5-dioctyloxybenzene (63 mg, 0.13 mmol), 4-(trifluoromethyl)phenylboronic acid (76 mg, 0.40 mmol), $Pd(PPh_3)_4$ (18 mg, 0.016 mmol), and Cs_2CO_3 (207 mg, 0.635 mmol) was degassed under vacuum, followed by a N_2 flow cycle repeated three times. Employing the same procedure as that described in the synthesis of compound **1**, product **2** was obtained as a white solid (72 mg, 90%). ^{1}H NMR (500 MHz, $CDCl_3$): δ_H 8.09 (d, J = 8.4 Hz, 4H), 7.67 (d, J = 8.4 Hz, 4H), 6.99 (s, 2H), 3.95 (s, 6H), 3.92 (t, J = 6.4 Hz, 4H), 1.68 (dt, J = 14.3, 6.5 Hz, 4H), 1.34 (t, J = 10.7 Hz, 4H), 1.25 (dq, J = 13.7, 8.4, 7.8 Hz, 16H), 0.87 (t, J = 7.0 Hz, 6H). ^{13}C NMR (125 MHz, $CDCl_3$): δ_C 150.4, 130.2, 130.0, 125.0 (two overlapping peaks), 116.1, 69.8, 31.9, 29.4, 29.3, 26.2, 22.8, 14.2. MS-APCI(+) (m/z): $[M]^+$ calcd for $C_{36}H_{44}F_6O_2$, 622.3240; found, 622.3244.

3. 1,4-Dioxane (5 mL) and H_2O (5 mL) were mixed and degassed using N_2. A mixture of 1,4-dibromo-2,5-dioctyloxybenzene (73 mg, 0.15 mmol), 4-cyanophenylboronic acid (63 mg, 0.43 mmol), $Pd(PPh_3)_4$ (22 mg, 0.019 mmol), and Cs_2CO_3 (224 mg, 0.687 mmol) was degassed under vacuum, followed by a N_2 flow cycle repeated three times. Employing the same procedure as that described in the synthesis of compound **1**, product **3** was obtained as a white solid (74 mg, 92%). ^{1}H NMR (500 MHz, $CDCl_3$): δ_H 7.70 (d, J = 1.1 Hz, 8H), 6.95 (s, 2H), 3.93 (t, J = 6.4 Hz, 4H), 1.68 (p, J = 6.5 Hz, 4H), 1.37−1.30 (m, 4H), 1.30−1.18 (m, 16H), 0.88 (t, J = 7.1 Hz, 6H). ^{13}C NMR (125 MHz, $CDCl_3$): δ_C 167.3, 150.5, 143.2, 130.5, 129.7, 129.4, 128.8, 116.1, 69.8, 52.2, 31.9, 29.4 (two overlapping peaks), 29.3, 26.2, 22.8, 14.2. MS-APCI(+) (m/z): $[M]^+$ calcd for $C_{36}H_{44}N_2O_2$, 536.3397; found, 536.3394.

4. 1,4-Dioxane (5 mL) and H_2O (5 mL) were mixed and degassed using N_2. A mixture of 1,4-dibromo-2,5-dioctyloxybenzene (77 mg, 0.16 mmol), 4-(methoxycarbonyl)phenylboronic acid (79 mg, 0.44 mmol), $Pd(PPh_3)_4$ (25 mg, 0.022 mmol), and Cs_2CO_3 (253 mg, 0.777 mmol) was degassed under vacuum, followed by a N_2 flow cycle repeated three times. The degassed solvent was then injected into the mixture. Employing the same procedure as that described in the synthesis of compound **1**, product **4** was obtained as a white solid (88 mg, 94%). ^{1}H NMR (500 MHz, $CDCl_3$): δ_H 7.69 (q, J = 8.4 Hz, 8H), 6.97 (s, 2H), 3.93 (t, J = 6.5 Hz, 4H), 1.68 (dt, J = 14.3, 6.5 Hz, 4H), 1.38−1.30 (m, 4H), 1.31−1.20 (m, 16H), 0.87 (t, J = 7.1 Hz, 6H). ^{13}C NMR (125 MHz, $CDCl_3$): δ_C 150.4, 143.0, 131.9, 130.3, 130.0, 119.2, 115.8, 110.9, 69.7, 31.9, 29.4, 29.3, 26.2, 22.8, 14.3. MS-ESI(+) (m/z): $[M + H]^+$ calcd for $C_{38}H_{51}O_6$, 603.3680; found, 603.3680; $[M + NH_4]^+$ calcd for $C_{38}H_{54}NO_6$, 620.3946; found, 620.3926; $[M + Na]^+$ calcd for $C_{38}H_{50}O_6Na$, 625.3500; found, 625.3488.

5. 1,4-Dioxane (10 mL) and H_2O (10 mL) were mixed and degassed using N_2. A mixture of 1,4-dibromo-2,5-dioctyloxybenzene (1003 mg, 2.04 mmol), 4-nitrophenylboronic acid (1365 mg, 8.18 mmol), $Pd(PPh_3)_4$ (397 mg, 0.344 mmol), and Cs_2CO_3 (3.83 g, 11.8 mmol) was degassed under vacuum, followed by a N_2 flow cycle repeated three times and the degassed solvent was injected into this mixture using a cannula. After reacting at 90 °C under a N_2 atmosphere for 24 h, the mixture was cooled to room temperature and the solvent was removed under reduced pressure. The remaining solid was dissolved in CH_2Cl_2 and mixed with Celite545 in preparation for purification by column chromatography (SiO_2, hexane/CH_2Cl_2 9:1) to afford product **5** as a yellow solid (995 mg, 85%). ^{1}H NMR (500 MHz, $CDCl_3$): δ_H 8.26 (d, J = 4.4, 1.0 Hz, 4H), 7.74 (d, J = 4.4, 2.0 Hz, 4H), 6.99 (s, 2H), 3.95 (t, J = 6.4 Hz, 4H), 1.69 (dt, J = 7.2, 3.4 Hz, 4H), 1.39−1.31 (m, 4H), 1.30−1.19 (m, 16H), 0.87 (t, J = 7.0 Hz, 6H). ^{13}C NMR (125 MHz, $CDCl_3$): δ_C 150.3, 146.8, 144.8, 130.3, 129.7, 123.3, 115.6, 69.6, 31.8, 29.2 (two overlapping peaks), 26.1, 22.6, 14.1. MS-ESI(+) (m/z): $[M + NH_4]^+$ calcd for $C_{34}H_{48}N_3O_6$, 594.3538; found, 594.3547; $[M + Na]^+$ calcd for $C_{34}H_{44}N_2O_6Na$, 599.3092; found, 599.3102.

6. 1,4-Dioxane (80 mL) and H_2O (80 mL) were mixed and degassed using N_2. A mixture of 1,4-dibromo-2,5-dimethoxybenzene (2.16 g, 7.30 mmol), 4-pyridineboronic acid (1.91 g, 15.5 mmol), $Pd(PPh_3)_4$ (856 mg, 0.741 mmol), and Cs_2CO_3 (6.04 g, 18.5 mmol) was degassed further using vacuum, followed by a N_2 flow cycle repeated three times and the degassed solvent was injected into this mixture using a cannula. Employing the same procedure as that described in the synthesis of compound **5**, product **6** was obtained as a yellow solid (1988 mg, 93%). ^{1}H NMR (500 MHz, $CDCl_3$): δ_H 8.67 (d, J = 5.1 Hz, 4H), 7.52 (d, J = 5.2 Hz, 4H), 7.00 (s, 2H), 3.83 (s, 6H). ESI-HRMS (m/z): $[M + H]^+$ calculated for $C_{18}H_{16}N_2O_2$, 293.1212; found, 293.1297.

7·2PF$_6$. A solution of **6** (101 mg, 0.35 mmol) and benzyl bromide (1.0 mL, 4.1 mmol) in a mixture of dry CH_2Cl_2 (20 mL) and MeCN (40 mL) was heated under reflux for 24 h. The precipitate was collected by filtration and washed with CH_2Cl_2 (3 × 20 mL). The precipitate was dissolved in anhydrous MeOH (100 mL) and the solution filtered, followed by the addition of NH_4PF_6. The resulting precipitate was isolated, washed with H_2O (2 × 30 mL), and dried in vacuo to obtain product **7**·2PF$_6$ as a yellow solid (195 mg, 89%). ^{1}H NMR (500 MHz, CD_3CN): δ_H 8.74 (d, J = 7.0 Hz, 4H), 8.34 (d, J = 7.0 Hz, 4H), 7.52 (s, 10H), 7.47 (d, J = 8.3 Hz, 4H), 7.33 (s, 2H), 5.75 (s, 4H), 3.93 (s, 6H). ESI-HRMS (m/z): $[M - PF_6]^+$ calcd for $C_{32}H_{30}F_6N_2O_2P$, 619.1944; found, 619.1947.

8·2PF$_6$. A solution of **6** (590 mg, 1.99 mmol) and *p*-xylylene dibromide (5.31 g, 20.1 mmol) in a mixture of dry CH_2Cl_2 (100 mL) and MeCN (200 mL) was heated under reflux for 24 h. The precipitate was collected by filtration and washed with CH_2Cl_2 (3 × 50 mL). The precipitate was then dissolved in anhydrous MeOH (300 mL) and the solution filtered, followed by the addition of NH_4PF_6. The resulting precipitate was isolated, washed with H_2O (2 × 80 mL), and dried in vacuo to obtain product **8**·2PF$_6$ as a yellow solid (1.55 g, 82%). ^{1}H NMR (500 MHz, CD_3CN): δ_H 8.75 (d, J = 7.0 Hz, 4H), 8.32 (d, J = 7.0 Hz, 4H), 7.55 (d, J = 8.3 Hz, 4H), 7.47 (d, J = 8.3 Hz, 4H), 7.31 (s, 2H), 5.72 (s, 4H), 4.61 (s, 4H), 3.91 (s, 6H). ESI-HRMS (m/z): $[M - PF_6]^+$ calcd for $C_{34}H_{32}Br_2N_2O_2F_{12}P_2$, 805.0446; found, 805.0446.

9·4PF$_6$. A solution of **6** (260 mg, 0.274 mmol), **8**·2PF$_6$ (80 mg, 0.274 mmol), and tetrabutylammonium iodide (TBAI) (18 mg, 0.056 mmol) in dry MeCN (200 mL) was heated under reflux for 3 days. After cooling to room temperature, excess of tetrabutylammonium chloride (TBACl) was added to quench the reaction, and the crude precipitate was subjected to reverse-phase C18 column chromatography, starting with H_2O/0.1% trifluoroacetic acid (TFA) as an eluent, followed by continuous addition of MeCN up to an eluent mixture of 99.9% MeCN/0.1% TFA. The fractions containing the product were combined and followed by removal of MeCN by rotary evaporation under vacuum. The resulting solid was dissolved in H_2O and treated with an excess of NH_4PF_6, affording a yellow precipitate, which was separated by filtration and dried in vacuo to obtain product **9**·4PF$_6$ as a yellow solid (124 mg, 33%). ^{1}H NMR (500 MHz, CD_3CN): δ_H 8.78 (d, J = 6.3 Hz, 8H), 8.19 (d, J = 6.3 Hz, 8H), 7.64 (s, 8H), 7.12 (s, 4H), 5.70 (s, 8H), 3.76 (s, 12H). ^{13}C NMR (125 MHz, CD_3CN): δ_C 154.9, 152.2, 144.4, 135.4, 130.6, 129.1, 127.5, 115.6, 63.8, 57.0. ESI-HRMS (m/z): $[M - 2PF_6]^{2+}$ calcd for $C_{52}H_{48}F_{12}N_4O_4P_2$, 541.1474; found, 541.1473.

UV/vis Absorption and Fluorescence Emission Spectroscopic Analyses. Fluorescent dyes were dissolved in the appropriate solvents to afford 1 mM solutions prior to spectroscopic analysis. A portion of 30 μL of a 1 mM solution was diluted by adding a selected solvent to a sample with a total volume of 3000 μL, affording a 1 × 10^{-5} M solution. UV/vis absorption spectra were recorded in glass cuvettes on a UV-3600 Shimadzu spectrophotometer. Steady-state

https://doi.org/10.1021/jacs.2c04906
J. Am. Chem. Soc. 2022, 144, 16841−16854

emission spectra were acquired in quartz cuvettes with optical pathlengths of 10 mm containing the solution being analyzed using a HORIBA FluoroMax 4 spectrofluorometer, which was equipped with an integrating sphere for determining the absolute photoluminescence quantum yield.

Steady-state and time-resolved emission spectra for dyes **7**·2PF_6 and **9**·4PF_6 were acquired using a HORIBA Fluorolog-3 spectrofluorometer, equipped with a time-correlated single photon counting module (diode laser excitation at λ = 375 nm) and an integrating sphere, which was used for absolute photoluminescence quantum yield determinations. Picosecond TRF measurements were recorded using a commercial direct-diode-pumped 100 kHz amplifier (Spirit 1040-HE, Spectra-Physics), producing a fundamental beam of 1040 nm (350 fs, 12 W) which was used to pump a non-collinear optical parametric amplifier (Spirit-NOPA, SpectraPhysics) capable of delivering tunable, high-repetition rate pulses with pulse widths as short as sub-20 fs. Samples **7**·2PF_6 and **9**·4PF_6 were excited with 340 nm, 2 nJ laser pulses. Fluorescence was detected using a Hamamatsu C4780 Streakscope as previously described in the literature.[71] Samples were prepared in 2 mm quartz cuvettes. All data were acquired in the single photon-counting mode using the Hamamatsu HPD-TA software. The temporal resolution was approximately 2% of the sweep window. Single wavelength kinetic analysis was performed using a nonlinear least-squares fit to a sum of exponentials convoluted with an instrument response function. Visible and near-infrared femtosecond and nanosecond transient absorption (TA) (fsTA and nsTA, respectively) spectroscopy were performed following descriptions already recorded in the literature.[58] The 330 nm, ~100 fs pump pulses were generated at 1 μJ per pulse using a commercial collinear optical parametric amplifier (TOPAS-Prime, Light-Conversion, Ltd.); 414-nm pump pulses were obtained by second-harmonic generation of the 828 nm fundamental. The pump polarization was randomized using a commercial depolarizer (DPU-25-A, Thorlabs, Inc.) to eliminate any orientational dynamics resulting from the experiment. Spectra were collected on commercial spectrometers (customized Ultrafast Systems Helios and EOS spectrometers, for fsTA and nsTA, respectively) for each time window. All samples were stirred to avoid localized heating or degradation effects. The optical density was maintained at 0.6 for all samples.

X-ray Crystallography. X-ray quality single crystals of dyes **1**−**5** were obtained by slow evaporation of CH_2Cl_2 solutions left open to the air at 298 K. The tetrakis(hexaflurophosphate) salt of tetracationic cyclophane $\mathbf{9}^{4+}$ was dissolved in MeCN at 298 K and the mixture was passed through a 0.45 μm filter separately into three 1-mL tubes. The tubes were placed together in a 20 mL vial containing $^{i}Pr_2O$ (~3 mL) and the vial was capped. Slow vapor diffusion of $^{i}Pr_2O$ into the solution of **9**·4PF_6 in MeCN over the course of a week yielded yellow single crystals. A suitable crystal was selected and it was mounted on a MITIGEN holder with Paratone oil on (i) a XtaLAB Synergy R, DW system, HyPix, or (ii) a Bruker and APEX-II CCD diffractometer. The X-ray single-crystal parameters for dyes **1**−**5** are listed in Table 1.

Cell Culture, Treatment, and Imaging. MCF-7 Breast cancer cells were grown in standard Dulbecco's modified eagle medium (DMEM), which was supplemented with 10% fetal bovine serum (FBS) and 1% penicillin−streptomycin (Corning). Cells were seeded into an 8-well imaging coverglass chamber (manufacturer-CellVis) or multiwell plate using phenol red free DMEM about 24 h prior to treatment. Dye **9**·4Cl was resuspended in deionized H_2O before being diluted to their final concentrations in the cell culture media. Cells were treated with the dye for 24 h prior to imaging. Uptake assays were carried out at concentrations from 1−50 μM, including a vehicle control (untreated). For the cell growth assays, cells were treated with the dye for 24 h at a range of concentrations from 0.1−50 μM.

Confocal imaging was performed on a Leica SP8 laser scanning confocal microscope on a DMi8 upright stand with LAS X software in the Biological Imaging Facility (BIF) at Northwestern University. Uptake images were taken with a 63×/1.4 NA objective, scanning at a zoom of two with a pinhole of one Airy unit at 600 Hz with a galvo scanner and line averaging of two. Images were 92.35 × 92.35 μm (1024 × 1024) with 10 slices in the z direction with a step size of 0.3 μm (total stack volume 3.0 μm). A single excitation wavelength (405 nm) was used at a power of approximately 14 μW. For the emission collection, a Leica spectral hybrid (HyD) detector set to collect a wavelength range of 500−650 nm (with a gain of 24%) was used. A transmitted light image was also collected simultaneously using the timeline photomultiplier (TL-PMT). Images were processed with FIJI/ImageJ (NIH) and settings were kept consistent throughout the series of images. Images presented are maximum intensity projections.

For the cell cytotoxicity experiments, MCF-7 cells were plated in a 96-well culture plate at a density of 0.01 × 10^6 cells per well in DMEM media with 10% FBS and 1% penicillin−streptomycin. Cells were cultured for 24 h before being treated with the dye at a range of concentrations from 0.1−50 μM. After treatment, cells were placed in a BioTek LionheartFX system, where they were imaged at 4× magnification every 3 h for 72 h under standard (37 °C, 5% CO_2) culture conditions. Phase contrast images were processed and analyzed with BioTek Gen5 analysis software to identify cell numbers at each time point during the culture period.

Table 1. X-ray Single-Crystal (Super)Structures of Dyes 1−5

dye	1	2	3	4	5
EWG	F	CF_3	CN	COOMe	NO_2
length/Å	14.1[e]	15.4	16.6	18.4[e]	15.4
width/Å	23.9	23.9	23.1	23.1	25.1
height/Å	1.60	1.54/1.96[f]	1.62	1.70	2.96
dihedral angles/deg	±42	+39/+51	±38	±38	±46
DR's[a] C-to-C[b] distance/Å	4.76	5.12	5.12	6.18	3.99
DR's P-to-P[c] distance/Å	3.64	3.50	3.96	3.62	3.76
DR's slip angle[73] θ/deg	50	43	51	36	70
AR's[d] C-to-C distance/Å	4.76	5.12	5.12	5.54[g]	3.99
AR's P-to-P distance/Å	NA[h]	NA	3.15	3.62	3.44
AR's slip angle θ/deg	NA	NA	51	36	60

[a]DR denotes donor ring. [b]C-to-C denotes centroid-to-centroid. [c]P-to-P denotes plane-to-plane. [d]AR denotes acceptor ring. [e]Lengths of the molecules when measured between two EWGs located at the termini do not correspond to the maximum lengths of the molecules because the two long *n*-octyloxy chains have non-perpendicular orientations with the *para*-terphenylene backbone, resulting in the overall lengths of the molecules extending beyond the two EWGs located at the termini. [f]Heights of the molecule are not the same because of the different dihedral angles between the adjacent aromatic rings. [g]C-to-C distance of AR is different from DR on account of the staggered [$\pi\cdots\pi$] packing pattern, which results from the closest C-to-C distances of adjacent ARs and DRs belonging to different molecules. [h]NA denotes the planar distance is not available because of the non-parallel orientation of the neighbor phenylene rings.

RESULTS AND DISCUSSION

The syntheses of fluorescent dyes **1**−**6**, **7**·2PF_6, **8**·2PF_6, and **9**·4PF_6 are shown in Scheme 1. For the syntheses of **1**−**5**, the precursor of the central *para*-phenylene rings—1,4-dibromo-2,5-dioctyloxylbenzene—was obtained (Scheme S1) from 1,4-dibromo-2,5-hydroquinone and 1-bromooctane. In order to attach two electron-deficient-substituted phenylene rings to both ends of a dioctyloxyphenylene unit located in the midriff, Suzuki couplings[72] between 1,4-dibromo-2,5-dioctyloxybenzene and (i) 4-fluorophenylboronic acid, (ii) 4-(trifluoromethyl)phenylboronic acid, (iii) 4-cyanophenylboronic acid, and (iv) 4-(methoxycarbonyl)phenylboronic acid, respectively, in H_2O/dioxane (1:1) were carried out (Scheme S2) at 100 °C under an N_2 atmosphere for 4 h in a

https://doi.org/10.1021/jacs.2c04906
J. Am. Chem. Soc. 2022, 144, 16841−16854

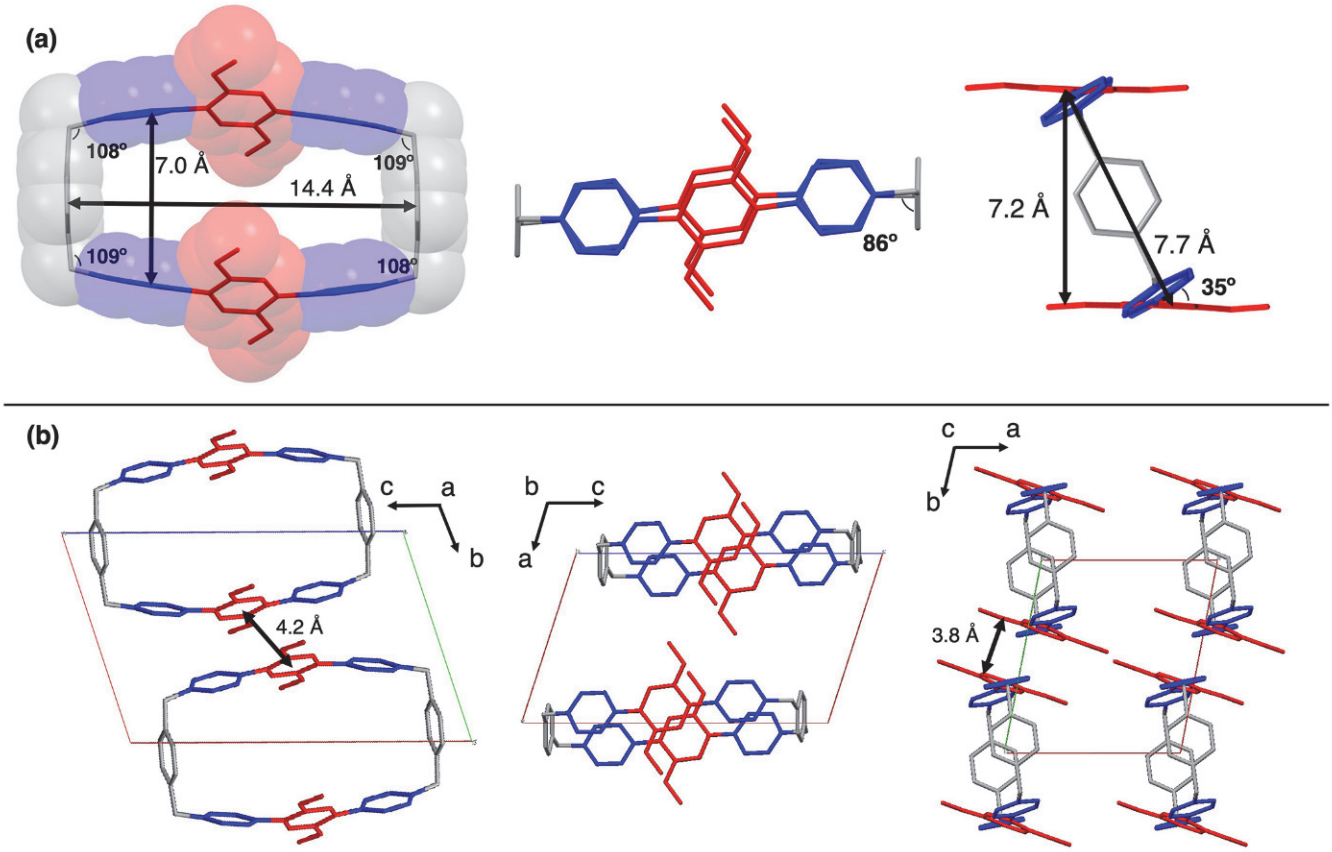

Figure 1. (a) Graphical representations of the solid-state structure of tetracationic cyclophane 9^{4+}. Plan view (left) of a stick representation with the corresponding semitransparent space-filling image superimposed upon it, showing distances and bond angles associated with the cyclophane's geometry. Side-on views (middle and right) of stick representations of 9^{4+}, illustrating the distances and dihedral angles associated with the cyclophane's geometry. (b) Plan views (left) of the solid-state superstructures of 9^{4+}, showing the centroid-to-centroid distance and side-on views (middle and right), illustrating the plane-to-plane distance between adjacent dimethoxyphenylene rings. Hydrogen atoms, solvents, and counterions are omitted for the sake of clarity.

microwave reactor, affording **1**−**4**, respectively. Dye **5** was obtained (Scheme S2) from a Suzuki coupling[72] of 1,4-dibromo-2,5-dioctyloxybenzene with 4-nitrophenylboronic acid at 90 °C under an N_2 atmosphere for 24 h after which dye **6** was obtained (Scheme S3) from the coupling of 1,4-dibromo-2,5-dimethyloxybenzene and 4-pyridinylboronic acid under the same conditions. Subsequently, S_N2 reactions in the presence of an excess of (i) benzyl bromide (Scheme S4) and (ii) α,α'-dibromo-*p*-xylene (Scheme S5) with **6** in CH_2Cl_2/MeCN (1:1) under refluxing conditions for 24 h, followed by counterion exchange with NH_4PF_6, resulted in the formation of dyes (i) **7**·2PF_6 and (ii) **8**·2PF_6, respectively. In the reaction (Scheme S6) involving the mixing of **6** and **8**·2PF_6 in a ratio of 1:1 in dry MeCN and in the presence of ∼20 mol % TBAI heating under reflux was followed by the addition of solid TBACl to precipitate the crude product. The crude product, which was subjected to reverse-phase C18 column chromatography, followed by counterion exchange with an excess of NH_4PF_6 in aqueous solution, produced a yellow precipitate. The product was separated by filtration and dried in vacuo to obtain the fluorescent cyclophane **9**·4PF_6. Water-soluble **9**·4Cl was obtained subsequently by counterion exchange in MeCN with an excess of TBACl, followed by a centrifugal separation. For more details of the synthesis, see Section B in the Supporting Information. Characterization of these compounds, which was carried out by ^{1}H and ^{13}C nuclear magnetic resonance (NMR) spectroscopy (Figures S1−S15) and high-resolution mass spectrometry (Figures S16−S23) (HRMS) is reported in Sections C and D, respectively, in the Supporting Information.

Further evidence for dye formation comes from single-crystal X-ray diffraction (XRD) analysis. X-ray quality single crystals of dyes **1**−**5** were obtained by slow evaporation of CH_2Cl_2 solutions left open to the air at 298 K. All single crystals had long needle-like shapes and exhibited a strong fluorescence under a UV (365 nm) lamp. The solid-state (super)structures of **1**−**5** are shown in Figures S65−S74. Some key structural data, such as molecular dimensions, dihedral angles between the adjacent (red and blue) *para*-phenylene rings, centroid-to-centroid (C-to-C), and plane-to-plane (P-to-P) distances as well as the slip angles[73] between a set of neighboring (i) electron-rich DRs (red) in their midriffs or (ii) electron-deficient ARs (blue) at their termini are shown in Table 1. The distance between two EWGs parallel to the long axis of the *para*-terphenylene backbone is defined as the length of the molecule. The width of the molecule is the projection (on the plane which is perpendicular to the axle of the backbone) distances between two terminal carbon atoms in the long *n*-octyloxy chains (green). The height of the molecule is the projection (on the plane of the DR) distances between two aromatic carbon atoms in the ARs. The parallel/antiparallel alignment of the long hydrophobic *n*-octyloxy chains reveals

https://doi.org/10.1021/jacs.2c04906
J. Am. Chem. Soc. 2022, 144, 16841−16854

that these interactions play a role in the alignment of the molecules in the superstructures. The plane-to-plane distances between sets of neighboring (i) electron-rich DRs (red) or (ii) electron-deficient ARs (blue) lie in the range of 3−4 Å, revealing their intermolecular [$\pi\cdots\pi$] stacking.

The density functional theory (DFT) calculated structural parameters are in good agreement (Table S3) with the single-crystal (super)structures in which dyes were optimized structurally using the crystal (super)structures as the sources of the molecular geometries. The calculated S_1 transition energies for each of dyes exhibit a good correlation with the electron-withdrawing strengths that influences the quadrupolarity of the π-conjugated *para*-terphenylene backbone. For both the monomers (Figure S75) and the dimers (Figure S76), the wavelengths of the calculated absorption bands (from the shortest to longest) are matched with the electron-withdrawing propensities (from the weakest to the strongest) of the terminal ARs. The CN-substituted and COOMe-substituted dyes **3** and **4** have similar calculated absorption and emission wavelengths, which correlate with the electron-withdrawing propensities of their EWGs. In order to visualize the interactions between the minimized structures of the dimers of dyes **1**−**5**, the independent gradient model based on the Hirshfeld partition of molecular density[74] (IGMH) method was used. This computational method plots (Figure S77) a surface representing noncovalent interactions between weakly interacting compounds. The IGMH plots confirm that the spatial pattern of interactions between the substituted *para*-terphenylene backbones depends on the relative orientations of the aromatic rings. In the case of dyes **1** and **2** (EWG = F and CF_3, respectively), the edge-to-face interactions between the terminal ARs of the dimers result in localized pockets of [CH$\cdots\pi$] interactions. Non-planar intermolecular co-conformations in the case of **1** and **2** may result from the lack of π-conjugation between their EWGs and aromatic rings. In the case of dyes **3** and **4** (EWG = CN and COOMe, respectively), the face-to-face overlapping between the ARs of the dimers is reflected in extensive [$\pi\cdots\pi$] interactions. The NO_2-substituted dye **5**, which exhibits the largest face-to-face overlap of all the minimized dimer structures, results in the most extensive surface representing [$\pi\cdots\pi$] stacking. Both XRD data and DFT calculations carried out on the solid-state superstructure of dye **5** reveal shorter C-to-C distances and greater slip angles[73] between aromatic rings, raising the possibility of its having significantly stronger [$\pi\cdots\pi$] stacking interactions compared with its analogues **1**−**4**.

A single crystal of the fluorescent tetracationic cyclophane **9**·$4PF_6$ was obtained by vapor diffusion of $^iPr_2O$ into a MeCN solution over the course of a week. The solid-state structure reveals (Figure 1a) a box-like tetracationic cyclophane, measuring 14.4 Å in length and 7.0 and 7.7 Å in width at its periphery and center, respectively. The two dihedral angles between the adjacent electron-deficient pyridinium and electron-rich dimethylphenylene rings are both 35°, resulting in a shorter distance (7.2 Å) as the P-to-P distance between two central rings, which is greater than the average dihedral angle[75] (∼30°) in $ExBox^{4+}$. The extended solid-state superstructure of $\mathbf{9}^{4+}$ reveals (Figure 1b) that the dimethylphenylene rings are facing each other, with a C-to-C distance of 3.8 Å and a P-to-P distance of 4.2 Å. The overall superstructure of $\mathbf{9}^{4+}$ reveals a parallel arrangement of the tetracationic cyclophanes. For more details of the XRD and the DFT calculation of the (super)structures, see Section H and I as well as CIF and MOL files in the Supporting Information.

Fluorescent dyes **1**−**6**, **7**·$2PF_6$, **8**·$2PF_6$, **9**·$4PF_6$, and **9**·4Cl were dissolved in tetrahydrofuran (THF) (**1**−**5**), MeCN (**6**, **7**·$2PF_6$, **8**·$2PF_6$ and **9**·$4PF_6$), and H_2O (**9**·4Cl), respectively, to afford 10 μM solutions prior to spectroscopic analysis. For comparison, their normalized (i) UV/vis absorption (Figure 2)

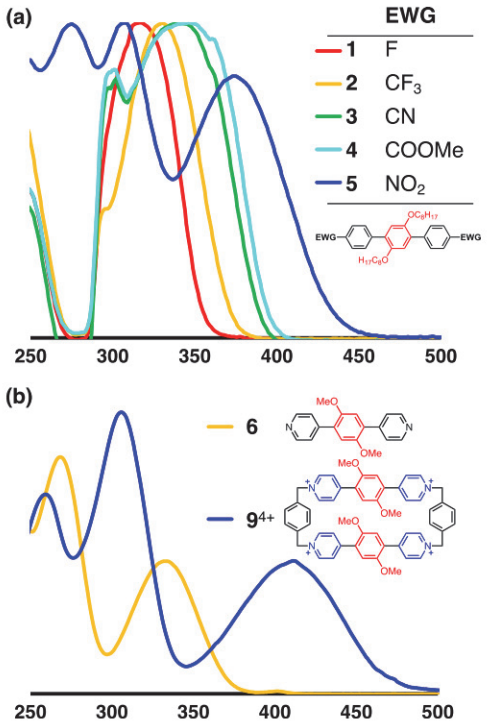

Figure 2. Overlay of the UV/vis absorption spectra of the quadrupolar fluorescent dyes. (a) Normalized peaks for **1** (red), **2** (orange), **3** (green), **4** (cyan), and **5** (blue) recorded in THF at 298 K. (b) Normalized peaks for **6** (orange) and **9**·$4PF_6$ (blue) recorded in MeCN at 298 K. Peaks have been normalized based on the absorption band maxima.

and (ii) the fluorescence emission (Figure 3) spectra of quadrupolar dyes are overlayed, displaying a large range of S_1 absorbance and emission maxima, which rely highly on their quadrupolarity that is correlated to the electron deficiency of the ARs.

For EWG-substituted dyes **1**−**5**, both their maximum S_1 absorption and emission wavelengths are correlated with a polar effect, an observation which depends on the electron-withdrawing propensities of their EWGs. F-Substituted dye **1** displays a deep violet emission (Figure S34) at λ_{em} = 380 nm, with a UV absorption band (Figure S24) centered on 316 nm. With the attachment of relatively stronger EWGs, that is, CF_3/CN/COOMe, respectively, **2**, **3**, and **4** display violet/blue emissions (Figures S35−S37) with bathochromic shifts in absorption (Figures S25−S27). All of dyes **1**−**4** exhibit weak or moderate solvatochromic effects (Figures S44−S47) that correlate with the strength of the EWGs as well. Moreover, dyes **3** and **4** have similar spectroscopic features in both absorption and emission spectra, resulting from their related EWGs. NO_2-Substituted dye **5** exhibits unique photophysical properties: in addition to having significant red-shifted absorption (Figure S28) and emission (Figure S38) bands, it also displays (Figure S48) a wider solvatochromic range and

https://doi.org/10.1021/jacs.2c04906
J. Am. Chem. Soc. 2022, 144, 16841−16854

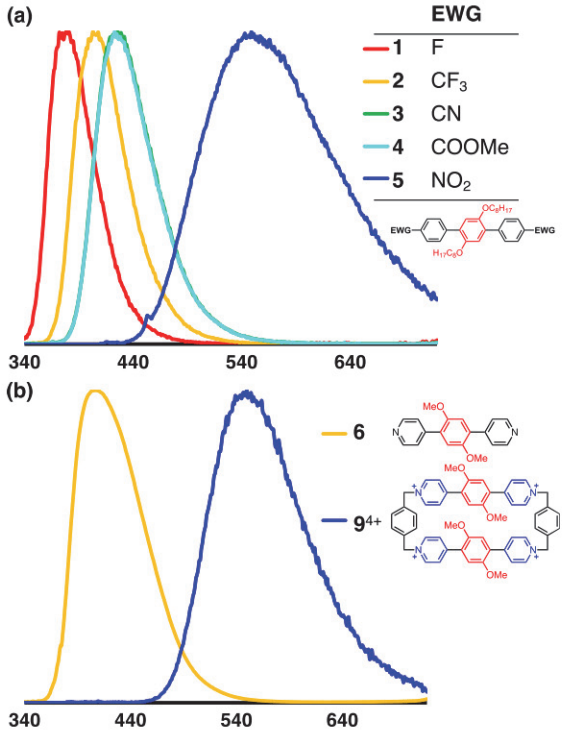

Figure 3. Overlay of the fluorescence emission spectra of the quadrupolar fluorescent dyes. (a) Normalized peaks for **1** (red), **2** (orange), **3** (green), **4** (cyan), and **5** (blue) recorded in THF. (b) Normalized peaks for **6** (orange) and **9**·4PF$_6$ (blue) recorded in MeCN. Peaks have been normalized based on the emission band maxima.

no fluorescence in some of nonprotic solvents with low polarities.

By comparing the absorbance and emission maxima of dyes **6**, **7**·2PF$_6$, **8**·2PF$_6$, **9**·4PF$_6$, and **9**·4Cl—where the pyridine and substituted pyridinium units act as the electron-deficient ARs—the wavelength−quadrupolarity correlation is confirmed. Dye **6** has similar absorption (Figure S29) and emission (Figure S39) properties to those of CF$_3$-substituted dye **2** as a result of similar electron deficiencies of their ARs. When the pyridines are quaternized to afford cationic pyridinium units, the polar effect is promoted dramatically, resulting in obvious bathochromic shifts in both the absorption (Figures S30−S33) and emission (Figures S40−S43) spectra. All the pyridinium-substituted dyes—namely, **7**·2PF$_6$, **8**·2PF$_6$, **9**·4PF$_6$, and **9**·4Cl—share a similar feature in their spectra, indicating that the quadrupolar extended-bipyridinium building block is the chromophore. The dramatic red shift in the absorption and emission of the pyridinium-containing series of dyes compared to pyridine-substituted dye **6** originates[76] most likely from substantial charge-transfer (CT) interactions between the pyridinium AR and dimethoxyphenylene DR, resulting in a CT absorption band (Figures S30−S33) with a maximum between 410 and 413 nm. They all emit in green light (~545 nm, Figures S40−S43) from this CT state. CT-interactions have been probed more deeply using time-resolved spectroscopy. For more details of UV/vis and fluorescence spectra, see Section E and F, respectively, in the Supporting Information.

The excited-state properties of these quadrupolar dyes were investigated using TA spectroscopy. The transient kinetics were analyzed globally and all time constants are given in Table S1. The TA data of dyes **1**−**4** and **6** in MeCN with λ_{ex} = 350 nm (Figures S49−S52 and S55) show similar spectra with the same general electronic evolution, though with differing kinetics. Following excitation, strong excited-state absorption features appear between ~450 and 500 nm along with a strong single peak in the near-infrared region, both of which are associated with $S_n \leftarrow S_1$ absorptions. The visible band red-shifts over the following ~100 ps, while the near-infrared band peaks first blue-shift in the initial ~10 ps before stabilizing. These near-infrared absorption bands are similar to those observed[59,60] in extended bipyridinium compounds. Following these shifts, the excited-state decay via emission with lifetimes between 3 and 4 ns as confirmed by TRF spectroscopy (Figures S58−S64). The spectral shape of the transient species is generally maintained throughout their lifetimes, implying that the dynamics in each dye all occur on a single electronic excited state (S_1) prior to emission. The spectral shifts at early times may arise due to excited-state symmetry-breaking[77,78] in the quadrupolar dyes, wherein fluctuations in the instantaneous electrostatic environment afforded by the solvent transiently favor wavefunction localization on one side of the symmetric molecule, creating an excited state with a large dipole moment that is associated with the Stokes shift observed[79] in the fluorescence spectra. This localization can lead to changes in the TA spectra as a result of the breakdown[42,80] of the Laporte rule. The shifts at longer times may arise from the solvent or structural relaxation of the dyes.

The fluorescence quantum yields (Φ_F) in solution generally increase with the strength of the EWG in dyes **1**−**4**. The total (relaxed) excited-state decay rates are much less sensitive to this effect, though a clear trend is observed when this rate is decomposed into its radiative (k_R) and non-radiative (k_R) contributions (Table S2). The radiative decay rate constants increase from k_R = (26 ns)$^{-1}$ to (4.9 ns)$^{-1}$ from **1** to **4**, consistent with the increase in Φ_F, though no obvious trend is seen in the non-radiative decay times. Dye **6** shows an intermediate k_R value, though one of the higher Φ_F in the series, despite the fact that the structural differences between **6** and the other dyes makes a comparison difficult.

NO$_2$-Substituted dye **5**, however, shows markedly different dynamics from the others in both MeCN (Figure S53) and PhMe (Figure S54) solutions, when excited at 350 nm. In the polar solvent MeCN, the initially excited state appearing near 380 nm is replaced by a strong peak at 505 nm in 4.3 ± 0.3 ps, which we attribute to CT involving the NO$_2$ group. This ultrafast S_1 decay is consistent with the measured near-zero Φ_F (Table S2). Following some relaxation, this CT state decays back to the ground state in 102 ns. In contrast, when excited in low-polarity solvent PhMe, dye **5** shows a more structured S_1 state that decays in 7.9 ± 0.3 ps to a different state with excited-state absorption peaks at 509 and ~700 nm. This state decays in 18 ns to a triplet state with a diffusional quenching-limited lifetime of 1 μs in a deaerated solution. The dramatic dependence on the solvent polarity and the modulation of lifetimes corroborates the assignment of this nanosecond-lived species is a CT state. The appearance of a triplet recombination product in PhMe also supports this claim, as the destabilization of the CT state in a lower-polarity solvent makes recombination to this state energetically feasible, unlike for the highly stabilized CT state in MeCN.

The Φ_F of **9**·4PF$_6$ and **9**·4Cl in the solid-state (powder) following 414 nm excitation were found to be 0.030 ± 0.005

https://doi.org/10.1021/jacs.2c04906
J. Am. Chem. Soc. 2022, 144, 16841−16854

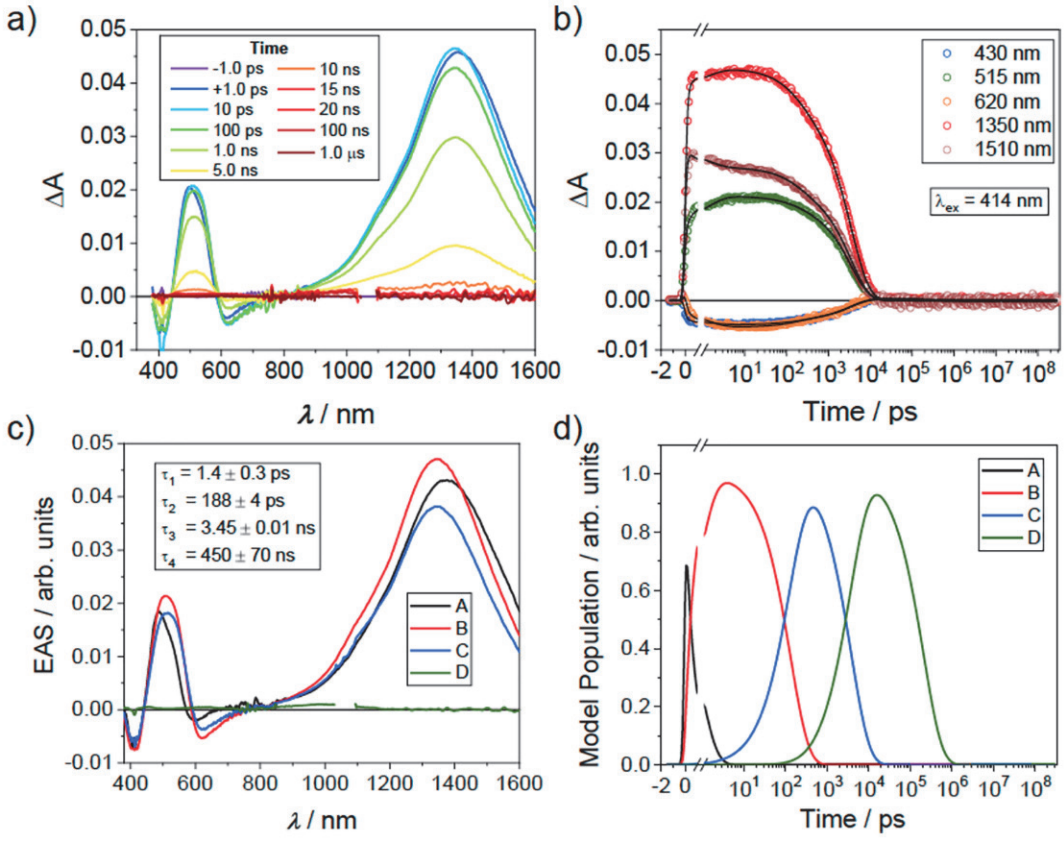

Figure 4. TA spectra of the tetracationic cyclophane. (a) Combined fs- and nsTA spectra of **9**·4PF$_6$ in MeCN at 298 K following a ~100 fs, 414 nm (1 μJ/pulse) excitation. (b) Multiple-wavelength fits and time constants from the fsTA for **9**·4PF$_6$ excited at 414 nm. (c) Evolution-associated spectra for an A → B → C → D → ground state sequential decay model. (d) Population model kinetic profiles.

and 0.016 ± 0.005, respectively. A similar decrease in Φ_F with the counterion was observed in the solution (0.28 for **9**·4PF$_6$ in MeCN compared to 0.15 for of **9**·4Cl in H_2O), suggesting that interactions with the chloride is abbreviating the excited-state lifetime. The order-of-magnitude decrease moving from solution to the solid state is most likely a result of the increased interactions between closely packed chromophores quenching the emission, as is commonly observed[81−84] in molecular solids.

The excited-state dynamics of the tetracationic cyclophane **9**·4PF$_6$ and its subunit **7**·2PF$_6$, which both contain extended bipyridinium units, are quite different from those of dyes **1**−**6** in MeCN. The TA spectra of **7**·2PF$_6$ (Figure S56) and **9**·4PF$_6$ (Figure 4), following excitation of their CT absorption bands at 414 nm, reveal the rapid appearance of strong excited-state absorption features at 506 and 1356 nm, as well as stimulated emission with an apparent minimum at 618 nm. The excited-state absorption features are similar to those[59] of ExBox^{4+}, though with the addition of a strong stimulated emission from radiative recombination (RR) of the CT state. This CT state is likely between the electron-donating dimethoxyphenylene unit and an adjacent electron-deficient pyridinium, as the same absorption and transient features are observed in both tetracationic cyclophane **9**·4PF$_6$ and its subunit **7**·2PF$_6$; there is no evidence of involvement[85] from the *para*-xylylene linker. The formation of a CT state from a symmetric A−D−A system also relies on excited-state symmetry breaking as discussed above, where the same fluctuations that induce wavefunction localization in the neutral dyes also favor charge separation along one side of the molecule. In the TA spectra, the minimum of the bleach is consistent with the red-shifted steady-state emission of both **7**·2PF$_6$ and **9**·4PF$_6$ in MeCN, distorted by the addition of a strong, positive excited-state absorption near 508 nm. These signals shift subtly and decay over the next several hundred picoseconds as the rigid tetracationic cyclophane **9**·4PF$_6$ (Figure S64) undergoes modest structural changes to accommodate the CT excited state, prior to decaying radiatively with a lifetime of 3.45 ± 0.01 ns. The lifetime of the dicationic **7**·2PF$_6$ (Figure S63) excited state is 8.78 ± 0.03 ns. Both lifetimes were again corroborated by TRF spectroscopy. The shorter lifetime exhibited by **9**·4PF$_6$ is most likely a consequence of the distortions forced upon the *para*-xylylene linkers by the box-like geometry of the tetracationic cyclophane. Indeed, while the radiative decay rate is quite similar between **7**·2PF$_6$ and **9**·4PF$_6$ in MeCN, the non-radiative rate in **9**·4PF$_6$ is more than seven times faster, resulting in the reduced Φ_F. Excitation of the dimethoxyphenylene-substituted extended bipyridinium units at 330 nm in both **7**·2PF$_6$ and **9**·4PF$_6$ yields very similar data to that from the direct excitation of the CT band, indicating that intramolecular CT occurs within the ~300 fs instrument response. Following decay of the CT state, a small amount of the triplet state forms, showing a weakly absorbing feature near 458 nm: more triplet is generated in **7**·2PF$_6$ than in **9**·4PF$_6$ for the simple reason that the longer CT state lifetime enables competition from intersystem crossing. In H_2O, tetracationic cyclophane **9**·4Cl (Figure S57) shows similar spectral features but with a shorter CT state lifetime (2.69 ± 0.02 ns), consistent with the reduced Φ_F (0.15) and no triplet formation in contrast to **9**·4PF$_6$ in MeCN, most

https://doi.org/10.1021/jacs.2c04906
J. Am. Chem. Soc. 2022, 144, 16841−16854

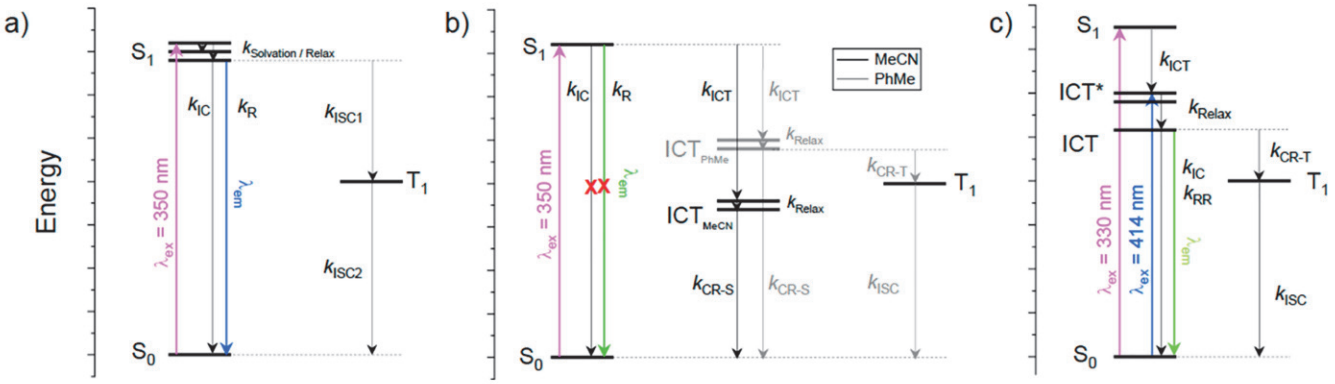

Figure 5. State diagrams for dyes (a) **1**−**4** and **6** in MeCN, (b) **5** in MeCN and PhMe, and (c) **7**·2PF$_6$ and **9**·4PF$_6$ in MeCN on the same energy scale showing competitive decay pathways: solvation and structural/vibrational relaxation (relax), non-radiative internal conversion (IC), radiative decay (fluorescence, R), intramolecular CT (ICT), radiative recombination (RR), charge recombination to singlet ground and triplet excited states (CR-S and CR-T, respectively), and intersystem crossing (ISC).

likely because of the short lifetime inhibiting spin mixing. While the decreased lifetime may be a result of the higher polarity aqueous environment,[60] a similar reduction in Φ_F was observed in the solid state discussed above, implying that the counterions may be playing an important role. Because the emission in $\mathbf{7}^{2+}$ and $\mathbf{9}^{4+}$ originates from a CT state, the electrostatic interactions of the different counterions with this state can alter recombination kinetics: indeed, in solution the non-radiative rate in **9**·4Cl decreases more than the concomitant increase in the radiative rate, while still yielding a faster overall decay than **9**·4PF$_6$ (Table S1). The dynamics of all dyes are summarized in Figure 5. For more details relating to the TA and TRF spectra, see Section G in the Supporting Information.

Small-molecule dyes are known[86] to intercalate with the DNA on account of electrostatic and base−pair interactions. The presence of these interactions inhibits enzyme function, elevating the cytotoxicity in living cells. To test the cytotoxicity of dye **9**·4Cl, we performed (Figure 6) a series of cell-uptake and viability experiments using MCF-7 breast cancer cells. When the cells were treated with **9**·4Cl at concentrations from 1−50 μM, we observed that the dye was readily taken up by cells. Moreover, the cells were viable and treatments of up to 10 μM concentration are non-cytotoxic for up to 64 h post-treatment. At low concentrations (up to 1 μM, Figure S78), the growth of the cells is comparable with that of non-treated control cells. Cell growth decreases gradually at concentrations of 5 μM and above. While cell growth appears impaired at higher concentrations, minimal cell death is observed.

Because of its low cytotoxicity and emission (Figure S43) in the green region (548 nm) at micromolar concentrations (Φ_F = 0.15), water-soluble **9**·4Cl was subjected to live-cell imaging with MCF-7 breast cancer cells. Living cells treated with the tetracationic cyclophane at 50 and 20 μM (Figure 7) and as low as 1 μM (Figure S78) concentrations, were imaged by laser scanning confocal microscopy. The dye fluoresces brightly in cells when excited with blue light (405 nm laser) and emits strongly in the green region (500−650 nm). As a result of the significantly low cytotoxicity profile of the cyclophane and the tolerance of cells for live-cell imaging at low concentrations, as well as its nanoconfined nature, **9**·4Cl holds out promise of applications such as (i) photoprotection and generation of singlet oxygen to kill cancer cells during photodynamic therapy and (ii) supramolecular drug encapsulation and subsequent release under the triggers of chemical stimuli or light. For more details of cell experiments, see Section J in the Supporting Information.

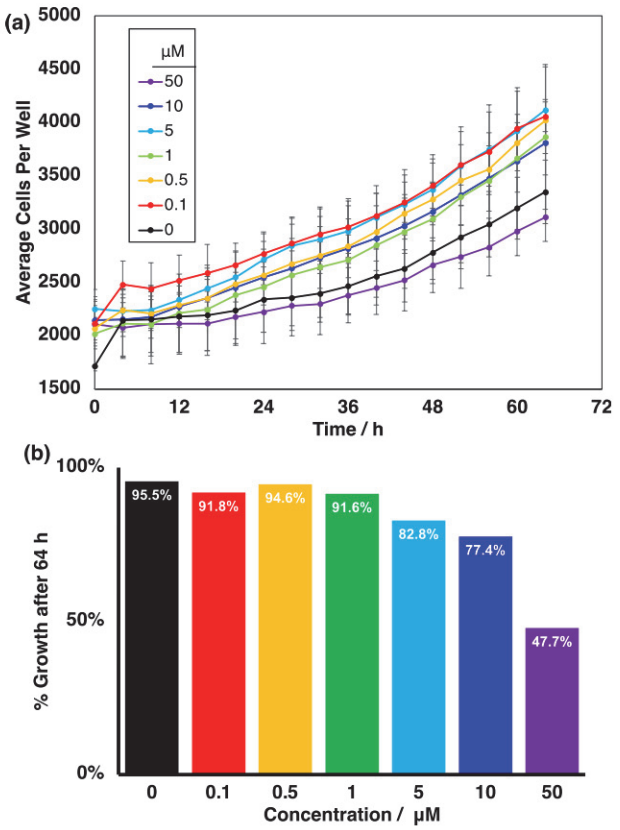

Figure 6. (a) Cell growth curves resulting from imaging every 4 h for 64 h under standard (37 °C, 5% CO_2) culture conditions. (b) Percentage growth after 64 h of incubations. Cells were seeded onto multiwell plates for 24 h and then treated with the dye at a range of concentrations from 0.1−50 μM and imaged for 64 h.

■ CONCLUSIONS

A series of fluorescent dyes, containing EWG-substituted *para*-terphenylene and extended-bipyridine/bipyridinium building blocks, has been designed and synthesized. By keeping the same alkoxy-substituted electron-rich phenylene rings in their

https://doi.org/10.1021/jacs.2c04906
J. Am. Chem. Soc. 2022, 144, 16841−16854

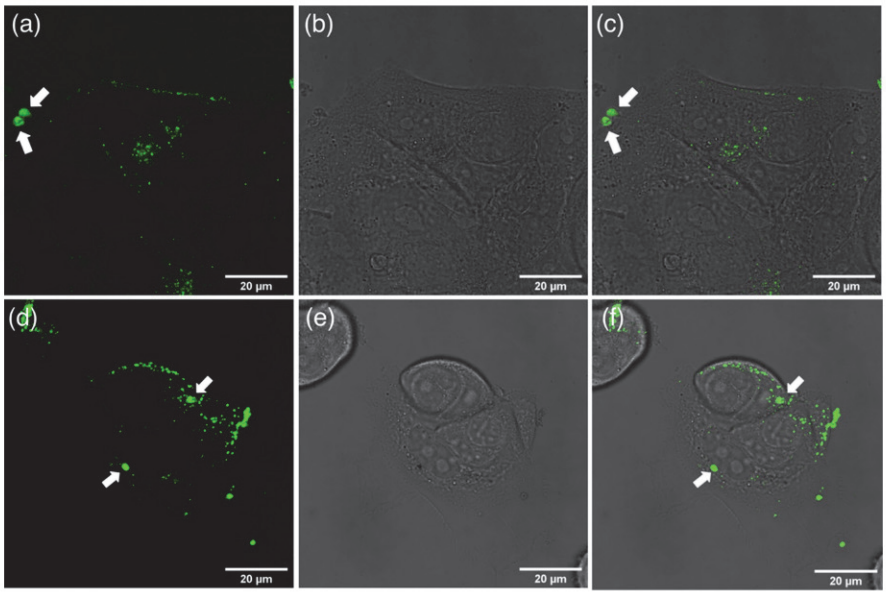

Figure 7. Cells treated with **9**·4Cl at 50 μM (a–c) and 10 μM (d–f) concentrations, respectively, for 24 h and imaged using laser scanning confocal microscopy. (a,d) Images of cells exhibiting green emission at 500–650 nm (λ_{ex} = 405 nm). (b,e) Transmitted light images. (c,f) Merged images showing the composite of emission and transmitted light images. Arrows pointed at dye **9**·4Cl were taken up by living cells and concentrated in intracellular compartments.

midriffs, the differences in the electron-deficient rings at their termini of the backbone influence their acceptor–donor–acceptor (A–D–A) quadrupolar arrays with modular molecular polarizabilities. Dyes **1** and **2**, which contain relatively weaker EWGs (i.e., F and CF_3, respectively) without π-conjugation, as well as the extended bipyridine-substituted **6**, result in their (i) higher S_1 transition energies, (ii) shorter wavelengths of fluorescence emission (λ_{em}) and UV/vis absorption (λ_{max}), and (iii) less pronounced solvatochromism. The ARs at the termini of **3** and **4** (EWG = CN and COOMe, respectively) have moderate electron deficiency, resulting in the dyes exhibiting relatively (i) lower S_1 transition energies, (ii) longer λ_{em} and λ_{max}, and (iii) more pronounced solvatochromism compared with **1** and **2**. Neutral dyes **1**–**4** and **6** in MeCN show similar TA spectra with the same general electronic evolution. The values of fluorescence quantum yields in solution generally increase with the strength of the EWG in dyes **1**–**4**, an observation which is consistent with radiative decay rate constants k_R. Dye **5**, which contains significantly stronger electron-withdrawing NO_2 groups on each of its ARs, displays dynamic photophysical behavior that is highly dependent on the nature of the solvent. It emits green light by absorbing blue light, eliciting red-shifted absorption and emission bands, as well as exhibiting a significant strong solvent effect: its λ_{em} has a relatively wide range in addition to the lack of fluorescence in low-polarity solvents. Its different dynamics when compared with the other neutral dyes have been revealed by TA spectroscopy in both MeCN and PhMe solutions.

Extended bipyridinium-substituted dyes 7^{2+}, 8^{2+}, and 9^{4+} all have cationic quadrupolar backbones in contrast to the original neutral extended bipyridine dye **6**. As a result of the electron-rich dimethoxyphenylene rings located in the midriffs of these cationic dyes, a more significant push–pull effect is produced, leading to a larger quadrupole. It follows that cationic dyes exhibit more pronounced red-shifted absorbance and emission maxima, rendering them similar to NO_2-substituted dye **5**. Single-crystal X-ray analysis of the tetracationic cyclophane 9^{4+} reveals a symmetrical rigid box-like structure with a cavity, in addition to strong intermolecular [$\pi\cdots\pi$] stacking interactions at the supramolecular level. Time-resolved femtosecond and nanosecond TA (fsTA and nsTA) and fluorescent emission (TRF) spectroscopy reveal intramolecular electron transfer between the dimethoxyphenylene and pyridinium rings in both linear 7^{2+} and box-like 9^{4+} following excitation of the CT absorption band at 414 nm. Spectra of the extended bipyridinium units, obtained on direct excitation at 330 nm of the CT bands in both 7^{2+} and 9^{4+}, display similar spectroscopic features, indicating that intramolecular CT occurs within the ~300 fs instrument response. We have demonstrated the non-cytotoxicity profile of water-soluble **9**·4Cl and obtained in vitro live-cell confocal microscopic images that demonstrate cell uptake at relatively low concentrations.

We hope this systematic investigation of A–D–A quadrupolar chromophores will inspire readers to design and synthesize new generations of organic fluorescent materials. The functionalized *para*-terphenylene and extended bipyridinium units constitute simple backbones that are easy to modify, making them excellent platforms to modulate and fine-tune their photophysical properties. Excited-state symmetry-breaking in centrosymmetric A–D–A dyes has been shown to correlate with large changes in the quadrupole moment in non-polar media and can be tuned[31] by modulating the electron acceptor, such as by using EWGs. The push–pull interactions between the electron-rich alkoxyphenylene midriff and the flanking EWG-substituted phenylene termini are also similar to the effects seen in non-fullerene acceptors in organic photovoltaic devices, such as those using indacenodithiophenes like ITIC,[87,88] where the magnitude of the quadrupole moment has been shown to correlate[89] with the charge-separation yield in organic photovoltaic devices. The push–pull effect can be further modulated[88] by the solvent, which has significant implications for its use in devices where the organic thin film produces a low-polarity environment that can

https://doi.org/10.1021/jacs.2c04906
J. Am. Chem. Soc. 2022, 144, 16841–16854

be altered[87,90] by the quadrupole moment of the surrounding chromophores. Thus, the quadrupole moment can play a determining role in the excited-state and charge-separation dynamics of these dyes. Furthermore, rigid box-like fluorescent cyclophanes[63] could incorporate appropriate photosensitizers to form host–guest complexes, which could lead to the development of stimuli-responsive photosensors capable of being used in photodynamic therapy in the treatment of cancer.

■ ASSOCIATED CONTENT

Supporting Information

The Supporting Information is available free of charge at https://pubs.acs.org/doi/10.1021/jacs.2c04906.

Calculated *XYZ* coordinates for geometric optimized data for **1** monomer (MOL)

Calculated *XYZ* coordinates for geometric optimized data for **2** monomer (MOL)

Calculated *XYZ* coordinates for geometric optimized data for **3** monomer (MOL)

Calculated *XYZ* coordinates for geometric optimized data for **4** monomer (MOL)

Calculated *XYZ* coordinates for geometric optimized data for **5** monomer (MOL)

Calculated *XYZ* coordinates for geometric optimized data for **1** dimer (MOL)

Calculated *XYZ* coordinates for geometric optimized data for **2** dimer (MOL)

Calculated *XYZ* coordinates for geometric optimized data for **3** dimer (MOL)

Calculated *XYZ* coordinates for geometric optimized data for **4** dimer (MOL)

Calculated *XYZ* coordinates for geometric optimized data for **5** dimer (MOL)

Chemical synthesis and characterization, NMR spectra, mass spectral data, UV/vis absorption spectra, fluorescence emission spectra, TA and TRF spectra, DFT calculations, X-ray crystal data, cell microscopic imaging, and cytotoxicity data (PDF)

Accession Codes

CCDC 2097203–2097207 and 2097209 contain the supplementary crystallographic data for this paper. These data can be obtained free of charge via www.ccdc.cam.ac.uk/data_request/cif, or by emailing data_request@ccdc.cam.ac.uk, or by contacting The Cambridge Crystallographic Data Centre, 12 Union Road, Cambridge CB2 1EZ, UK; fax: +44 1223 336033.

■ AUTHOR INFORMATION

Corresponding Author

J. Fraser Stoddart − *Department of Chemistry, Northwestern University, Evanston, Illinois 60208, United States; School of Chemistry, University of New South Wales, Sydney 2052 New South Wales, Australia; Stoddart Institute of Molecular Science, Department of Chemistry, Zhejiang University, Hangzhou 310027, China; ZJU-Hangzhou Global Scientific and Technological Innovation Center, Hangzhou 311215, China;* orcid.org/0000-0003-3161-3697; Phone: (+1)-847-491-3793; Email: stoddart@northwestern.edu

Authors

Yuanning Feng − *Department of Chemistry, Northwestern University, Evanston, Illinois 60208, United States;* orcid.org/0000-0002-8832-0767

Partha Jyoti Das − *Department of Chemistry, Northwestern University, Evanston, Illinois 60208, United States*

Ryan M. Young − *Department of Chemistry, Northwestern University, Evanston, Illinois 60208, United States; Institute for Sustainability and Energy at Northwestern, Northwestern University, Evanston, Illinois 60208, United States;* orcid.org/0000-0002-5108-0261

Paige J. Brown − *Department of Chemistry, Northwestern University, Evanston, Illinois 60208, United States; Institute for Sustainability and Energy at Northwestern, Northwestern University, Evanston, Illinois 60208, United States;* orcid.org/0000-0002-2934-0098

Jessica E. Hornick − *Chemistry for Life Processes Institutes and Department of Molecular Biosciences, Northwestern University, Evanston, Illinois 60208, United States*

Jacob A. Weber − *Department of Chemistry, Northwestern University, Evanston, Illinois 60208, United States*

James S. W. Seale − *Department of Chemistry, Northwestern University, Evanston, Illinois 60208, United States;* orcid.org/0000-0001-8086-6020

Charlotte L. Stern − *Integrated Molecular Structure Education and Research Center, Northwestern University, Evanston, Illinois 60208, United States;* orcid.org/0000-0002-9491-289X

Michael R. Wasielewski − *Department of Chemistry, Northwestern University, Evanston, Illinois 60208, United States; Institute for Sustainability and Energy at Northwestern, Northwestern University, Evanston, Illinois 60208, United States;* orcid.org/0000-0003-2920-5440

Complete contact information is available at: https://pubs.acs.org/10.1021/jacs.2c04906

Notes

The authors declare the following competing financial interest(s): Y.F. and J.F.S. have filed a patent application lodged with Northwestern University (INVO Reference No. NU 2022-141) based on this work.

■ ACKNOWLEDGMENTS

The authors thank Chenjian Lin for his assistance with the solid-state fluorescence quantum yield measurements and Drs Yang Jiao and Han Han for insightful discussions. The authors also thank Northwestern University (NU) for their support of this research. Time-resolved absorption and emission spectroscopy were supported by the National Science Foundation (DMR-2003739) (R.M.Y., P.J.B., and M.R.W.). Cell cytotoxicity and imaging were performed at the Biological Imaging Facility at Northwestern University (RRID:SCR_017767), generously supported by the Chemistry for Life Processes Institute, the Department of Molecular Biosciences, the Rice Foundation, and the NU Office for Research (J.E.H.). This research made use of the Integrated Molecular Structure Education and Research Center (IMSERC) NMR, MS, and X-ray facility at NU, which receives support from the Soft and Hybrid Nanotechnology Experimental (SHyNE) Resource (NSF ECCS-2025633) and NU (C.L.S.).

REFERENCES

(1) Li, D.; Guo, C.; Zhang, X.; Du, B.; Wang, P.; Cheng, S.; Cai, J.; Wang, H.; Liu, D.; Yao, H.; Hou, J.; Wang, T. Heating-Induced Aggregation Control for Efficient Sequential-Cast Organic Solar Cells. *Aggregate* **2022**, *3*, No. e104.

(2) Mata, G.; Luedtke, N. W. Synthesis and Solvatochromic Fluorescence of Biaryl Pyrimidine Nucleosides. *Org. Lett.* **2013**, *15*, 2462−2465.

(3) Klymchenko, A. S.; Mely, Y. Fluorescent Environment-Sensitive Dyes as Reporters of Biomolecular Interactions. *Prog. Mol. Biol. Transl. Sci.* **2013**, *113*, 35−58.

(4) Cornec, A.-S.; Baudequin, C.; Fiol-Petit, C.; Plé, N.; Dupas, G.; Ramondenc, Y. One "Click" to Access Push−Triazole−Pull Fluorophores Incorporating a Pyrimidine Moiety: Structure−Photophysical Properties Relationships. *Eur. J. Org. Chem.* **2013**, *2013*, 1908−1915.

(5) Jacquart, A.; Williams, R. M.; Brouwer, A. M.; Ishow, E. Decoupling Fluorescence and Photochromism in Bifunctional Azo Derivatives for Bulk Emissive Structures. *Chem.—Eur. J.* **2012**, *18*, 3706−3720.

(6) Dong, Y.; Bolduc, A.; McGregor, N.; Skene, W. G. Push−Pull Aminobithiophenes—Highly Fluorescent Stable Fluorophores. *Org. Lett.* **2011**, *13*, 1844−1847.

(7) Loving, G. S.; Sainlos, M.; Imperiali, B. Monitoring Protein Interactions and Dynamics with Solvatochromic Fluorophores. *Trends Biotechnol.* **2010**, *28*, 73−83.

(8) Qian, X.; Xiao, Y. 4-Amino-1,8-dicyanonaphthalene Derivatives as Novel Fluorophore and Fluorescence Switches: Efficient Synthesis and Fluorescence Enhancement Induced by Transition Metal Ions and Protons. *Tetrahedron Lett.* **2002**, *43*, 2991−2994.

(9) Ventelon, L.; Blanchard-Desce, M.; Moreaux, L.; Mertz, J. New Quadrupolar Fluorophores with High Two-Photon Excited Fluorescence. *Chem. Commun.* **1999**, 2055−2056.

(10) Hardin, B. E.; Snaith, H. J.; McGehee, M. D. The Renaissance of Dye-Sensitized Solar Cells. *Nat. Photonics* **2012**, *6*, 162−169.

(11) Mishra, A.; Fischer, M. K. R.; Bäuerle, P. Metal-Free Organic Dyes for Dye-Sensitized Solar Cells: From Structure: Property Relationships to Design Rules. *Angew. Chem., Int. Ed.* **2009**, *48*, 2474−2499.

(12) Ning, Z.; Tian, H. Triarylamine: A Promising Core Unit for Efficient Photovoltaic Materials. *Chem. Commun.* **2009**, 5483−5495.

(13) Huang, C.; Sartin, M. M.; Siegel, N.; Cozzuol, M.; Zhang, Y.; Hales, J. M.; Barlow, S.; Perry, J. W.; Marder, S. R. Photo-Induced Charge Transfer and Nonlinear Absorption in Dyads Composed of a Two-Photon-Absorbing Donor and a Perylene Diimide Acceptor. *J. Mater. Chem.* **2011**, *21*, 16119−16128.

(14) Kim, K. S.; Noh, S. B.; Katsuda, T.; Ito, S.; Osuka, A.; Kim, D. Charge Transfer Induced Enhancement of Near-IR Two-Photon Absorption of 5,15-Bis(azulenylethynyl) Zinc(II) Porphyrins. *Chem. Commun.* **2007**, 2479−2481.

(15) Min, H.; Park, I. S.; Yasuda, T. Dipolar and Quadrupolar Luminophores Based on 1,8-Dimethylcarbazole−Triazine Conjugates for High-Efficiency Blue Thermally Activated Delayed Fluorescence OLEDs. *ChemPhotoChem* **2020**, *4*, 82−88.

(16) Mukhopadhyay, S.; Topham, B. J.; Soos, Z. G.; Ramasesha, S. Neutral and Charged Excited States in Polar Organic Films: Origin of Unusual Electroluminescence in Tri-*p*-tolylamine-Based Hole Conductors. *J. Phys. Chem. A* **2008**, *112*, 7271−7279.

(17) Soos, Z. G.; Mukhopadhyay, S.; Ramasesha, S. Polar Organic Films: Transport Gap, Charge−Dipole Interaction and Electroluminescence of Tritolylamine (TTA) Derivatives. *Chem. Phys. Lett.* **2007**, *442*, 285−288.

(18) Shirota, Y. Photo- and Electroactive Amorphous Molecular Materials—Molecular Design, Syntheses, Reactions, Properties, and Applications. *J. Mater. Chem.* **2005**, *15*, 75−93.

(19) Ooyama, Y.; Matsugasako, A.; Oka, K.; Nagano, T.; Sumomogi, M.; Komaguchi, K.; Imae, I.; Harima, Y. Fluorescence PET (Photo-Induced Electron Transfer) Sensors for Water Based on Anthracene−Boronic Acid Ester. *Chem. Commun.* **2011**, *47*, 4448−4450.

(20) de Silva, A. P.; Moody, T. S.; Wright, G. D. Fluorescent PET (Photoinduced Electron Transfer) Sensors as Potent Analytical Tools. *Analyst* **2009**, *134*, 2385−2393.

(21) Griesbeck, S.; Michail, E.; Rauch, F.; Ogasawara, H.; Wang, C.; Sato, Y.; Edkins, R. M.; Zhang, Z.; Taki, M.; Lambert, C.; Yamaguchi, S.; Marder, T. B. The Effect of Branching on One- and Two-Photon Absorption, Cell Viability and Localization of Cationic Triarylborane Chromophores with Dipolar vs. Octupolar Charge Distributions for Cellular Imaging. *Chem.—Eur. J.* **2019**, *25*, 13164−13175.

(22) Didier, P.; Ulrich, G.; Mély, Y.; Ziessel, R. Improved Push-Pull-Push *E*-Bodipy Fluorophores for Two-Photon Cell-Imaging. *Org. Biomol. Chem.* **2009**, *7*, 3639−3642.

(23) Lord, S. J.; Conley, N. R.; Lee, H.-l. D.; Nishimura, S. Y.; Pomerantz, A. K.; Willets, K. A.; Lu, Z.; Wang, H.; Liu, N.; Samuel, R.; Weber, R.; Semyonov, A.; He, M.; Twieg, R. J.; Moerner, W. E. DCDHF Fluorophores for Single-Molecule Imaging in Cells. *ChemPhysChem* **2009**, *10*, 55−65.

(24) Lord, S. J.; Conley, N. R.; Lee, H.-L. D.; Samuel, R.; Liu, N.; Twieg, R. J.; Moerner, W. E. A Photoactivatable Push−Pull Fluorophore for Single-Molecule Imaging in Live Cells. *J. Am. Chem. Soc.* **2008**, *130*, 9204−9205.

(25) Chen, X.-Y.; Liu, Z.-Q.; Zhao, C.-H. Two-Photon Excited Fluorescent 3,3′-Diamino-5,5′-Diboryl-2,2′-Bithienyls Featuring a Quadrupolar Structure. *Chem.—Eur. J.* **2022**, *28*, No. e202104432.

(26) Berger, S. M.; Marder, T. B. Applications of Triarylborane Materials in Cell Imaging and Sensing of Bio-relevant Molecules such as DNA, RNA, and Proteins. *Mater. Horiz.* **2022**, *9*, 112−120.

(27) Berger, S. M.; Rühe, J.; Schwarzmann, J.; Phillipps, A.; Richard, A.-K.; Ferger, M.; Krummenacher, I.; Tumir, L.-M.; Ban, Ž.; Crnolatac, I.; Majhen, D.; Barišić, I.; Piantanida, I.; Schleier, D.; Griesbeck, S.; Friedrich, A.; Braunschweig, H.; Marder, T. B. Bithiophene-Cored, *mono-*, *bis-*, and *tris-*(Trimethylammonium)-Substituted, *bis*-Triarylborane Chromophores: Effect of the Number and Position of Charges on Cell Imaging and DNA/RNA Sensing. *Chem.—Eur. J.* **2021**, *27*, 14057−14072.

(28) Griesbeck, S.; Michail, E.; Wang, C.; Ogasawara, H.; Lorenzen, S.; Gerstner, L.; Zang, T.; Nitsch, J.; Sato, Y.; Bertermann, R.; Taki, M.; Lambert, C.; Yamaguchi, S.; Marder, T. B. Tuning the π-Bridge of Quadrupolar Triarylborane Chromophores for One- and Two-Photon Excited Fluorescence Imaging of Lysosomes in Live Cells. *Chem. Sci.* **2019**, *10*, 5405−5422.

(29) Rout, Y.; Montanari, C.; Pasciucco, E.; Misra, R.; Carlotti, B. Tuning the Fluorescence and the Intramolecular Charge Transfer of Phenothiazine Dipolar and Quadrupolar Derivatives by Oxygen Functionalization. *J. Am. Chem. Soc.* **2021**, *143*, 9933−9943.

(30) Ban, Ž.; Griesbeck, S.; Tomić, S.; Nitsch, J.; Marder, T. B.; Piantanida, I. A Quadrupolar Bis-Triarylborane Chromophore as a Fluorimetric and Chirooptic Probe for Simultaneous and Selective Sensing of DNA, RNA and Proteins. *Chem.—Eur. J.* **2020**, *26*, 2195−2203.

(31) Szakács, Z.; Tasior, M.; Gryko, D. T.; Vauthey, E. Change of Quadrupole Moment upon Excitation and Symmetry Breaking in Multibranched Donor-Acceptor Dyes. *ChemPhysChem* **2020**, *21*, 1718−1730.

(32) Dereka, B.; Svechkarev, D.; Rosspeintner, A.; Aster, A.; Lunzer, M.; Liska, R.; Mohs, A. M.; Vauthey, E. Solvent Tuning of Photochemistry Upon Excited-State Symmetry Breaking. *Nat. Commun.* **2020**, *11*, 1925.

(33) Ferger, M.; Ban, Ž.; Krošl, I.; Tomić, S.; Dietrich, L.; Lorenzen, S.; Rauch, F.; Sieh, D.; Friedrich, A.; Griesbeck, S.; Kenđel, A.; Miljanić, S.; Piantanida, I.; Marder, T. B. Bis(phenylethynyl)arene Linkers in Tetracationic bis-Triarylborane Chromophores Control Fluorimetric and Raman Sensing of Various DNA and RNA. *Chem.—Eur. J.* **2021**, *27*, 5142−5159.

(34) Amini, H.; Ban, Ž.; Ferger, M.; Lorenzen, S.; Rauch, F.; Friedrich, A.; Crnolatac, I.; Kenđel, A.; Miljanić, S.; Piantanida, I.; Marder, T. B. Tetracationic Bis-triarylborane 1,3-Butadiyne as a Combined Fluorimetric and Raman Probe for Simultaneous and

https://doi.org/10.1021/jacs.2c04906
J. Am. Chem. Soc. 2022, 144, 16841−16854

Selective Sensing of Various DNA, RNA and Proteins. *Chem.—Eur. J.* **2020**, *26*, 6017−6028.
(35) Griesbeck, S.; Zhang, Z.; Gutmann, M.; Lühmann, T.; Edkins, R. M.; Clermont, G.; Lazar, A. N.; Haehnel, M.; Edkins, K.; Eichhorn, A.; Blanchard-Desce, M.; Meinel, L.; Marder, T. B. Water-Soluble Triarylborane Chromophores for One- and Two-Photon Excited Fluorescence Imaging of Mitochondria in Cells. *Chem.—Eur. J.* **2016**, *22*, 14701−14706.
(36) Söderberg, M.; Dereka, B.; Marrocchi, A.; Carlotti, B.; Vauthey, E. Ground-State Structural Disorder and Excited-State Symmetry Breaking in a Quadrupolar Molecule. *J. Phys. Chem. Lett.* **2019**, *10*, 2944−2948.
(37) Dereka, B.; Vauthey, E. Direct Local Solvent Probing by Transient Infrared Spectroscopy Reveals the Mechanism of Hydrogen-Bond Induced Nonradiative Deactivation. *Chem. Sci.* **2017**, *8*, 5057−5066.
(38) Dereka, B.; Rosspeintner, A.; Stężycki, R.; Ruckebusch, C.; Gryko, D. T.; Vauthey, E. Excited-State Symmetry Breaking in a Quadrupolar Molecule Visualized in Time and Space. *J. Phys. Chem. Lett.* **2017**, *8*, 6029−6034.
(39) Dereka, B.; Koch, M.; Vauthey, E. Looking at Photoinduced Charge Transfer Processes in the IR: Answers to Several Long-Standing Questions. *Acc. Chem. Res.* **2017**, *50*, 426−434.
(40) Susumu, K.; Fisher, J. A. N.; Zheng, J.; Beratan, D. N.; Yodh, A. G.; Therien, M. J. Two-Photon Absorption Properties of Proquinoidal D-A-D and A-D-A Quadrupolar Chromophores. *J. Phys. Chem. A* **2011**, *115*, 5525−5539.
(41) Sissa, C.; Terenziani, F.; Painelli, A.; Abbotto, A.; Bellotto, L.; Marinzi, C.; Garbin, E.; Ferrante, C.; Bozio, R. Dimers of Quadrupolar Chromophores in Solution: Electrostatic Interactions and Optical Spectra. *J. Phys. Chem. B* **2010**, *114*, 882−893.
(42) Terenziani, F.; Painelli, A.; Katan, C.; Charlot, M.; Blanchard-Desce, M. Charge Instability in Quadrupolar Chromophores: Symmetry Breaking and Solvatochromism. *J. Am. Chem. Soc.* **2006**, *128*, 15742−15755.
(43) Antipov, I. F.; Ivanov, A. I. Effect of Symmetry Breaking in Excited Quadrupole Molecules on Transition Dipole Moment. *J. Phys. Chem. B* **2021**, *125*, 13778−13788.
(44) Zhang, W.; Xu, W.; Zhang, G.; Kong, J.; Niu, X.; Chan, J. M. W.; Liu, W.; Xia, A. Direct Tracking Excited-State Intramolecular Charge Redistribution of Acceptor−Donor−Acceptor Molecule by Means of Femtosecond Stimulated Raman Spectroscopy. *J. Phys. Chem. B* **2021**, *125*, 4456−4464.
(45) Chung, H. Y.; Oh, J.; Park, J.-H.; Cho, I.; Yoon, W. S.; Kwon, J. E.; Kim, D.; Park, S. Y. Spectroscopic Studies on Intramolecular Charge-Transfer Characteristics in Small-Molecule Organic Solar Cell Donors: A Case Study on ADA and DAD Triad Donors. *J. Phys. Chem. C* **2020**, *124*, 18502−18512.
(46) Ricci, F.; Carlotti, B.; Keller, B.; Bonaccorso, C.; Fortuna, C. G.; Goodson, T.; Elisei, F.; Spalletti, A. Enhancement of Two-Photon Absorption Parallels Intramolecular Charge-Transfer Efficiency in Quadrupolar versus Dipolar Cationic Chromophores. *J. Phys. Chem. C* **2017**, *121*, 3987−4001.
(47) Woo, H. Y.; Liu, B.; Kohler, B.; Korystov, D.; Mikhailovsky, A.; Bazan, G. C. Solvent Effects on the Two-Photon Absorption of Distyrylbenzene Chromophores. *J. Am. Chem. Soc.* **2005**, *127*, 14721−14729.
(48) Le Droumaguet, C.; Mongin, O.; Werts, M. H. V.; Blanchard-Desce, M. Towards "Smart" Multiphoton Fluorophores: Strongly Solvatochromic Probes for Two-Photon Sensing of Micropolarity. *Chem. Commun.* **2005**, 2802−2804.
(49) Wu, C.-J. J.; Xue, C.; Kuo, Y.-M.; Luo, F.-T. Preparation and Photoluminescence of *p*-Terphenyl Derivatives Containing Cyano Groups. *Tetrahedron* **2005**, *61*, 4735−4741.
(50) Kole, G. K.; Košćak, M.; Amar, A.; Majhen, D.; Božinović, K.; Brkljaca, Z.; Ferger, M.; Michail, E.; Lorenzen, S.; Friedrich, A.; Krummenacher, I.; Moos, M.; Braunschweig, H.; Boucekkine, A.; Lambert, C.; Halet, J.-F.; Piantanida, I.; Müller-Buschbaum, K.; Marder, T. B. Methyl Viologens of Bis-(4′-pyridylethynyl)arenes-Structures, Photophysical and Electrochemical Studies, and their Potential Application in Biology. *Chem.—Eur. J.* **2022**, *28*, No. e202200753.
(51) Fudickar, W.; Bauch, M.; Ihmels, H.; Linker, T. DNA-Triggered Enhancement of Singlet Oxygen Production by Pyridinium Alkynylanthracenes. *Chem.—Eur. J.* **2021**, *27*, 13591−13604.
(52) Kole, G. K.; Merz, J.; Amar, A.; Fontaine, B.; Boucekkine, A.; Nitsch, J.; Lorenzen, S.; Friedrich, A.; Krummenacher, I.; Košćak, M.; Braunschweig, H.; Piantanida, I.; Halet, J.-F.; Müller-Buschbaum, K.; Marder, T. B. 2- and 2,7-Substituted *para-N*-Methylpyridinium Pyrenes: Syntheses, Molecular and Electronic Structures, Photophysical, Electrochemical, and Spectroelectrochemical Properties and Binding to Double Stranded (ds)-DNA. *Chem.—Eur. J.* **2021**, *27*, 2837−2853.
(53) Ye, Z.; Yang, W.; Wang, C.; Zheng, Y.; Chi, W.; Liu, X.; Huang, Z.; Li, X.; Xiao, Y. Quaternary Piperazine-Substituted Rhodamines with Enhanced Brightness for Super-Resolution Imaging. *J. Am. Chem. Soc.* **2019**, *141*, 14491−14495.
(54) Pun, A. B.; Campos, L. M.; Congreve, D. N. Tunable Emission from Triplet Fusion Upconversion in Diketopyrrolopyrroles. *J. Am. Chem. Soc.* **2019**, *141*, 3777−3781.
(55) Goujon, A.; Colom, A.; Straková, K.; Mercier, V.; Mahecic, D.; Manley, S.; Sakai, N.; Roux, A.; Matile, S. Mechanosensitive Fluorescent Probes to Image Membrane Tension in Mitochondria, Endoplasmic Reticulum, and Lysosomes. *J. Am. Chem. Soc.* **2019**, *141*, 3380−3384.
(56) Signorini, R.; Ferrante, C.; Pedron, D.; Zerbetto, M.; Cecchetto, E.; Slaviero, M.; Fortunati, I.; Collini, E.; Bozio, R.; Abbotto, A.; Beverina, L.; Pagani, G. A. Effective Two-Photon Absorption Cross Section of Heteroaromatic Quadrupolar Dyes: Dependence on Measurement Technique and Laser Pulse Characteristics. *J. Phys. Chem. A* **2008**, *112*, 4224−4234.
(57) Abbotto, A.; Beverina, L.; Bozio, R.; Facchetti, A.; Ferrante, C.; Pagani, G. A.; Pedron, D.; Signorini, R. Novel Heterocycle-Based Two-Photon Absorbing Dyes. *Org. Lett.* **2002**, *4*, 1495−1498.
(58) Young, R. M.; Dyar, S. M.; Barnes, J. C.; Juríček, M.; Stoddart, J. F.; Co, D. T.; Wasielewski, M. R. Ultrafast Conformational Dynamics of Electron Transfer in $ExBox^{4+}$⊂Perylene. *J. Phys. Chem. A* **2013**, *117*, 12438−12448.
(59) Dyar, S. M.; Barnes, J. C.; Juríček, M.; Stoddart, J. F.; Co, D. T.; Young, R. M.; Wasielewski, M. R. Electron Transfer and Multi-Electron Accumulation in $ExBox^{4+}$. *Angew. Chem., Int. Ed.* **2014**, *53*, 5371−5375.
(60) Dale, E. J.; Vermeulen, N. A.; Juríček, M.; Barnes, J. C.; Young, R. M.; Wasielewski, M. R.; Stoddart, J. F. Supramolecular Explorations: Exhibiting the Extent of Extended Cationic Cyclophanes. *Acc. Chem. Res.* **2016**, *49*, 262−273.
(61) Ryan, S. T. J.; Young, R. M.; Henkelis, J. J.; Hafezi, N.; Vermeulen, N. A.; Hennig, A.; Dale, E. J.; Wu, Y.; Krzyaniak, M. D.; Fox, A.; Nau, W. M.; Wasielewski, M. R.; Stoddart, J. F.; Scherman, O. A. Energy and Electron Transfer Dynamics within a Series of Perylene Diimide/Cyclophane Systems. *J. Am. Chem. Soc.* **2015**, *137*, 15299−15307.
(62) Gong, X.; Young, R. M.; Hartlieb, K. J.; Miller, C.; Wu, Y.; Xiao, H.; Li, P.; Hafezi, N.; Zhou, J.; Ma, L.; Cheng, T.; Goddard, W. A., III; Farha, O. K.; Hupp, J. T.; Wasielewski, M. R.; Stoddart, J. F. Intramolecular Energy and Electron Transfer within a Diazaperopyrenium-Based Cyclophane. *J. Am. Chem. Soc.* **2017**, *139*, 4107−4116.
(63) Roy, I.; David, A. H. G.; Das, P. J.; Pe, D. J.; Stoddart, J. F. Fluorescent Cyclophanes and their Applications. *Chem. Soc. Rev.* **2022**, *51*, 5557−5605.
(64) Roy, I.; Bobbala, S.; Zhou, J.; Nguyen, M. T.; Nalluri, S. K. M.; Wu, Y.; Ferris, D. P.; Scott, E. A.; Wasielewski, M. R.; Stoddart, J. F. ExTzBox: A Glowing Cyclophane for Live-Cell Imaging. *J. Am. Chem. Soc.* **2018**, *140*, 7206−7212.
(65) Liu, W.; Tan, Y.; Jones, L. O.; Song, B.; Guo, Q.-H.; Zhang, L.; Qiu, Y.; Feng, Y.; Chen, X.-Y.; Schatz, G. C.; Stoddart, J. F. PCage:

Fluorescent Molecular Temples for Binding Sugars in Water. *J. Am. Chem. Soc.* **2021**, *143*, 15688−15700.
(66) Liu, W.; Bobbala, S.; Stern, C. L.; Hornick, J. E.; Liu, Y.; Enciso, A. E.; Scott, E. A.; Stoddart, J. F. XCage: A Tricyclic Octacationic Receptor for Perylene Diimide with Picomolar Affinity in Water. *J. Am. Chem. Soc.* **2020**, *142*, 3165−3173.
(67) Garci, A.; Weber, J. A.; Young, R. M.; Kazem-Rostami, M.; Ovalle, M.; Beldjoudi, Y.; Atilgan, A.; Bae, Y. J.; Liu, W.; Jones, L. O.; Stern, C. L.; Schatz, G. C.; Farha, O. K.; Wasielewski, M. R.; Stoddart, J. F. Mechanically Interlocked Pyrene-Based Photocatalysts. *Nat. Catal.* **2022**, *5*, 524−533.
(68) Garci, A.; Beldjoudi, Y.; Kodaimati, M. S.; Hornick, J. E.; Nguyen, M. T.; Cetin, M. M.; Stern, C. L.; Roy, I.; Weiss, E. A.; Stoddart, J. F. Mechanical-Bond-Induced Exciplex Fluorescence in an Anthracene-Based Homo[2]catenane. *J. Am. Chem. Soc.* **2020**, *142*, 7956−7967.
(69) Gong, X.; Zhou, J.; Hartlieb, K. J.; Miller, C.; Li, P.; Farha, O. K.; Hupp, J. T.; Young, R. M.; Wasielewski, M. R.; Stoddart, J. F. Toward a Charged Homo[2]catenane Employing Diazaperopyrenium Homophilic Recognition. *J. Am. Chem. Soc.* **2018**, *140*, 6540−6544.
(70) Juríček, M.; Barnes, J. C.; Strutt, N. L.; Vermeulen, N. A.; Ghooray, K. C.; Dale, E. J.; McGonigal, P. R.; Blackburn, A. K.; Avestro, A.-J.; Stoddart, J. F. An ExBox[2]Catenane. *Chem. Sci.* **2014**, *5*, 2724−2731.
(71) Chen, M.; Krzyaniak, M. D.; Nelson, J. N.; Bae, Y. J.; Harvey, S. M.; Schaller, R. D.; Young, R. M.; Wasielewski, M. R. Quintet-Triplet Mixing Determines the Fate of the Multiexciton State Produced by Singlet Fission in a Terrylenediimide Dimer at Room Temperature. *Proc. Natl. Acad. Sci. U.S.A.* **2019**, *116*, 8178−8183.
(72) Miyaura, N.; Suzuki, A. Palladium-Catalyzed Cross-Coupling Reactions of Organoboron Compounds. *Chem. Rev.* **1995**, *95*, 2457−2483.
(73) The slip angles (θ) were calculated by the arcsine function according to their P-to-P and C-to-C distances. θ = arccos(P-to-P/C-to-C).
(74) Lu, T.; Chen, Q. Independent Gradient Model Based on Hirshfeld Partition: A New Method for Visual Study of Interactions in Chemical Systems. *J. Comput. Chem.* **2022**, *43*, 539−555.
(75) Barnes, J. C.; Juríček, M.; Strutt, N. L.; Frasconi, M.; Sampath, S.; Giesener, M. A.; McGrier, P. L.; Bruns, C. J.; Stern, C. L.; Sarjeant, A. A.; Stoddart, J. F. ExBox: A Polycyclic Aromatic Hydrocarbon Scavenger. *J. Am. Chem. Soc.* **2013**, *135*, 183−192.
(76) Wu, Y.; Zhou, J.; Nelson, J. N.; Young, R. M.; Krzyaniak, M. D.; Wasielewski, M. R. Covalent Radical Pairs as Spin Qubits: Influence of Rapid Electron Motion between Two Equivalent Sites on Spin Coherence. *J. Am. Chem. Soc.* **2018**, *140*, 13011−13021.
(77) Vauthey, E. Photoinduced Symmetry-Breaking Charge Separation. *ChemPhysChem* **2012**, *13*, 2001−2011.
(78) Coleman, A. F.; Chen, M.; Zhou, J.; Shin, J. Y.; Wu, Y.; Young, R. M.; Wasielewski, M. R. Reversible Symmetry-Breaking Charge Separation in a Series of Perylenediimide Cyclophanes. *J. Phys. Chem. C* **2020**, *124*, 10408−10419.
(79) Lippert, E. Spektroskopische Bestimmung des Dipolmomentes aromatischer Verbindungen im ersten angeregten Singulettzustand. *Z. Elektrochem.* **1957**, *61*, 962−975.
(80) Szakács, Z.; Vauthey, E. Excited-State Symmetry Breaking and the Laporte Rule. *J. Phys. Chem. Lett.* **2021**, *12*, 4067−4071.
(81) Wang, S.; Miao, Y.; Yan, X.; Ye, K.; Wang, Y. A Dibenzo[a,c]phenazine-11,12-dicarbonitrile (DBPzDCN) Acceptor Based Thermally Activated Delayed Fluorescent Compound for Efficient Near-Infrared Electroluminescent Devices. *J. Mater. Chem. C* **2018**, *6*, 6698−6704.
(82) Wang, C.; Li, Z. Molecular Conformation and Packing: Their Critical Roles in the Emission Performance of Mechanochromic Fluorescence Materials. *Mater. Chem. Front.* **2017**, *1*, 2174−2194.
(83) Wang, S.; Yan, X.; Cheng, Z.; Zhang, H.; Liu, Y.; Wang, Y. Highly Efficient Near-Infrared Delayed Fluorescence Organic Light Emitting Diodes Using a Phenanthrene-Based Charge-Transfer Compound. *Angew. Chem., Int. Ed.* **2015**, *54*, 13068−13072.
(84) Englman, R.; Jortner, J. The Energy Gap Law for Radiationless Transitions in Large Molecules. *Mol. Phys.* **1970**, *18*, 145−164.
(85) Wu, Y.; Zhou, J.; Phelan, B. T.; Mauck, C. M.; Stoddart, J. F.; Young, R. M.; Wasielewski, M. R. Probing Distance Dependent Charge-Transfer Character in Excimers of Extended Viologen Cyclophanes Using Femtosecond Vibrational Spectroscopy. *J. Am. Chem. Soc.* **2017**, *139*, 14265−14276.
(86) Suseela, Y. V.; Das, S.; Pati, S. K.; Govindaraju, T. Imidazolyl-Naphthalenediimide-Based Threading Intercalators of DNA. *ChemBioChem* **2016**, *17*, 2162−2171.
(87) Umeyama, T.; Igarashi, K.; Sasada, D.; Tamai, Y.; Ishida, K.; Koganezawa, T.; Ohtani, S.; Tanaka, K.; Ohkita, H.; Imahori, H. Efficient Light-Harvesting, Energy Migration, and Charge Transfer by Nanographene-Based Nonfullerene Small-Molecule Acceptors Exhibiting Unusually Long Excited-State Lifetime in the Film State. *Chem. Sci.* **2020**, *11*, 3250−3257.
(88) Eastham, N. D.; Logsdon, J. L.; Manley, E. F.; Aldrich, T. J.; Leonardi, M. J.; Wang, G.; Powers-Riggs, N. E.; Young, R. M.; Chen, L. X.; Wasielewski, M. R.; Melkonyan, F. S.; Chang, R. P. H.; Marks, T. J. Hole-Transfer Dependence on Blend Morphology and Energy Level Alignment in Polymer: ITIC Photovoltaic Materials. *Adv. Mater.* **2018**, *30*, 1704263.
(89) Saladina, M.; Simón Marqués, P.; Markina, A.; Karuthedath, S.; Wöpke, C.; Göhler, C.; Chen, Y.; Allain, M.; Blanchard, P.; Cabanetos, C.; Andrienko, D.; Laquai, F.; Gorenflot, J.; Deibel, C. Charge Photogeneration in Non-Fullerene Organic Solar Cells: Influence of Excess Energy and Electrostatic Interactions. *Adv. Funct. Mater.* **2021**, *31*, 2007479.
(90) Ramirez, C. E.; Chen, S.; Powers-Riggs, N. E.; Schlesinger, I.; Young, R. M.; Wasielewski, M. R. Symmetry-Breaking Charge Separation in the Solid State: Tetra(phenoxy)perylenediimide Polycrystalline Films. *J. Am. Chem. Soc.* **2020**, *142*, 18243−18250.

https://doi.org/10.1021/jacs.2c04906
J. Am. Chem. Soc. 2022, 144, 16841−16854